Targeting Norepinephrine Neurons of the Locus Coeruleus: A Comparison of Model Systems and Strategies

Chantal Wissing[1,2*], Lena S. Eschholz[1,3*], Maxime Maheu[1,4], Kathrin Sauter[1], Fabio Morellini[5], Simon Wiegert[1,3#], Alexander Dieter[1,3#]

[1]*Synaptic Wiring Lab, Center for Molecular Neurobiology, University Medical Center Hamburg-Eppendorf, Hamburg, Germany*
[2]*Institute for Systems Physiology, Faculty of Medicine, University Clinic, Cologne, Germany*
[3]*Department of Neurophysiology, MCTN, Medical Faculty Mannheim, Heidelberg University, Mannheim, Germany*
[4]*Section Computational Cognitive Neuroscience, Department of Neurophysiology and Pathophysiology, University Medical Center Hamburg-Eppendorf, Hamburg, Germany*
[5]*Research Group Behavioral Biology, Center for Molecular Neurobiology, University Medical Center Hamburg-Eppendorf, Hamburg, Germany*

*equal contribution, #shared correspondence:
simon.wiegert@medma.uni-heidelberg.de, alexander.dieter@medma.uni-heidelberg.de

Keywords

Locus coeruleus, Norepinephrine, Noradrenaline, viral transduction, ectopic expression, *Dbh*^{cre}, *Net*^{cre}, *Th*^{cre}, PRS×8, fiber photometry

Highlights

- Heterogeneous expression patterns with different targeting strategies for LC-NE neurons
- Substantial ectopic transgene expression observed in some approaches
- No behavioral alterations in heterozygous cre mice as compared to wild-types
- PRS×8-driven reporter proteins and calcium indicators as a resource to investigate LC function

Abstract

The locus coeruleus (LC) norepinephrine (NE) system is involved in a variety of physiological and pathophysiological processes. Refining our understanding of LC function largely relies on selective transgene expression in molecularly defined cells, allowing targeted manipulation and readout of noradrenergic neurons. Here, we performed a side-by-side comparison of the most commonly used strategies to genetically target the LC, including different cre driver lines and promoter-mediated transgene expression. We report differences between these strategies in terms of transgene expression efficacy and molecular specificity. Notably, we found no behavioral alterations in cre-expressing mice of any mouse line compared to wild-type littermates. Finally, to further facilitate the investigation of LC-NE function, we have created a suite of constructs, including reporter proteins and calcium indicators in two different spectra, whose expression is mediated by the previously described PRS×8 promoter. These constructs allow identification and monitoring of LC-NE activity either in wild-type mice, or in combination with tissue-specific manipulations of different cre driver lines. The results of our study are crucial for the interpretation of previous experiments using the respective targeting strategies, as well as for the design of future studies.

Introduction

The locus coeruleus (LC) — a bilateral nucleus located in the brainstem — is the major source of norepinephrine (NE; also: noradrenaline) in the central nervous system. Despite its small size (~3,000 neurons in the rodent brain[1]), the LC is involved in several physiological functions, including alertness, arousal, sensory perception, attention, learning, and memory consolidation[2–4]. In addition, the LC has been implicated in numerous pathological conditions including depression, post-traumatic stress disorder, Alzheimer's disease, and Parkinson's disease[2–6].

Accordingly, the LC-NE system is currently the subject of detailed investigations[2,3,7–9]. Recent research suggests a high modularity of this nucleus, with subpopulations of cells targeting different brain regions, presumably with different physiological roles[2]. Thus, the LC may exert a more sophisticated, target-specific modulation of brain activity than previously thought. These findings have brought the LC-NE system into the focus of many research groups that rely on the specific targeting of LC-NE neurons to interrogate LC function[2]. Key technologies to access the LC-NE system in animal models include genetic tools such as cre driver lines (Supplementary Table S1) and viral transduction, either with conditional constructs, or with tissue-specific promoters. These methods allow gene expression in molecularly identified neural populations, even in a projection-specific manner[10]. Detailed studies of the LC-NE system are more feasible than ever with the recent development of genetically encoded sensors for norepinephrine[11,12] and dopamine[13–15], and opto- or

chemogenetic strategies that allow the manipulation of LC subpopulations in a projection-specific manner. Driver lines have been developed to express cre recombinase under the control of the dopamine-β-hydroxylase (DBH) promoter in mice[16,17] and rats[18], under control of the norepinephrine transporter (NET) in mice[19], and several mouse[16,20,21] and rat[22] driver lines exist that express cre recombinase under the control of the tyrosine hydroxylase (TH) promoter. DBH catalyzes the synthesis of NE from dopamine (DA) and is therefore specific for NE neurons. Similarly, NET, the membrane protein that mediates reuptake of extracellular NE, is used as a selective marker for NE-releasing neurons. In contrast, TH is the enzyme involved in the synthesis of L-DOPA from tyrosine, three reaction steps upstream of the end product NE, and is therefore present in all catecholaminergic cells, including dopaminergic ones.

Alternative approaches to target the LC-NE system that do not rely on transgenic lines have also been proposed. In particular, NE-specific transgene expression has been achieved using a minimal synthetic promoter, containing 8 copies of a cis-regulatory element (Phox2a/Phox2b response site; PRS) derived from the human *Dbh* promoter, thus termed PRS×8[23]. This promoter has been shown to be specific for noradrenergic cells in both mice[24,25] and rats[23,26]. While the four strategies (*Dbh*^{cre}, *Net*^{cre}, *Th*^{cre}, and PRS×8) for targeting of the LC-NE system provide a wide range of alternatives to choose from, they come with different caveats and challenges (see e.g., [27–29] for reviews on transgene expression strategies). Critically, a direct comparison of the most commonly used LC-NE targeting strategies is lacking, and proper quantification of viral transduction is not always reported.

Here, we performed a side-by-side comparison of virus-mediated transgene expression in the LC-NE system by introducing cre-dependent reporter genes into the LC of *Dbh*^{cre}, *Net*^{cre}, and *Th*^{cre} mice, and unconditional reporter genes under the control of the PRS×8-promoter into the LC of wild-type mice. We report substantial differences in transgene expression, both in terms of efficacy and molecular specificity, while we did not detect any behavioral changes associated with cre expression in any of the mouse lines tested. To facilitate investigations of the LC-NE system, we have developed a suite of PRS×8-driven fluorophores and calcium indicators that allow tissue-specific transgene expression either in wild-type mice, or in combination with cre driver lines, facilitating simultaneous transgene expression in additional neuronal populations. Our findings have broad implications for researchers using genetic manipulation of the noradrenergic system to study LC function: they may guide the choice of an appropriate targeting strategy in future research, and may help in the interpretation of data obtained from the respective model system.

Results

Efficacy and specificity of transgene expression

To visualize transgene expression in the LC-NE system, we bilaterally injected the LC with titer-matched suspensions of recombinant adeno-associated virus (rAAV2/9) encoding the

enhanced green fluorescent protein (eGFP; Fig. 1a). In *Dbh*^{cre}, *Net*^{cre} and *Th*^{cre} mice, cre-dependent gene expression was controlled by combining double-floxed inverted open reading frames (DIO)[30] of the transgene with a strong, synthetic promotor (CAG)[31]. In wild-type mice (C57BL/6J), the reporter gene was expressed under the control of the synthetic PRS×8 promoter. Six weeks after injection, we analyzed eGFP expression by fluorescence microscopy of coronal sections which were immuno-stained against TH (to visualize NE-expressing neurons) and GFP (to enhance the signal originating from transgene expression; Fig. 1b). To quantify transgene expression at a cellular level, cells expressing TH (TH$^+$) or eGFP (eGFP$^+$) were automatically segmented using the deep learning-based algorithm *CellPose*[32,33] (Fig. 1c).

To assess the ability to selectively target the LC, we evaluated the *efficacy* and *specificity* of viral transduction of LC-NE neurons. To this end, we compared the overlap between masks segmented in the TH and GFP channel, respectively, defining cells with an overlap of ≥ 50% as co-expressing. Efficacy is defined as the proportion of TH$^+$ cells co-expressing eGFP, while specificity reports the proportion of eGFP$^+$ cells co-expressing TH.

We found differences in the efficacy between model systems (one-way ANOVA, $F_{24} = 14.71$, $p = 1.2 \times 10^{-5}$; Fig. 1d, y-axis): while no significant differences in efficacy were detected between *Dbh*^{cre}, *Net*^{cre} and PRS×8-mediated transgene expression (70.5 ± 11.8 %, 79.5 ± 9.0 %, 78.2 ± 12.9 %; mean ± SD; Tukey's test, p = 0.68/0.77/0.99 for *Dbh*^{cre} vs *Net*^{cre}/*Dbh*^{cre} vs PRS×8/*Net*^{cre} vs PRS×8), the efficacy of *Th*^{cre} mediated expression was significantly lower than the other model systems (33.3 ± 22.7%; Tukey's test, $p = 6 \times 10^{-4}/3 \times 10^{-5}/5 \times 10^{-5}$, compared against *Dbh*^{cre}/*Net*^{cre}/PRS×8, respectively).

We also found differences in specificity (one-way ANOVA, $F_{24} = 14.47$, $p = 1.4 \times 10^{-5}$) between model systems (Fig. 1d, x-axis). Here, the specificity of *Th*^{cre} mediated expression (46.0 ± 12.1 %) was significantly lower than *Dbh*^{cre} (82.2 ± 9.5 %), *Net*^{cre} (71.4 ± 13.6 %), and PRS×8 (65.2 ± 5.0 %) mediated transgene expression (Tukey's test, $p = 7 \times 10^{-6}/ 7 \times 10^{-4}/0.01$ *Dbh*^{cre}/*Net*^{cre}/PRS×8 against *Th*^{cre}). Furthermore, the *Dbh*^{cre} approach was significantly more specific than PRS×8 mediated transgene expression (Tukey's test, p = 0.03). No significant differences were found between *Dbh*^{cre} vs. *Net*^{cre} and between PRS×8 vs. *Net*^{cre}.

We summarized efficacy and specificity into a single metric termed 'transduction efficiency', which is formally equivalent to the area under the receiver-operator curve (ROC), or to the average of efficacy and specificity. Transduction efficiency was different across groups (one-way ANOVA, $F_{24} = 19.65$, $p = 1.2 \times 10^{-6}$; Fig. 1e): *Dbh*^{cre}, *Net*^{cre}, and PRS×8 induced a more efficient transduction than *Th*^{cre} (difference to *Dbh*^{cre} = 36.7% ± 13.4%, Tukey's test, $p = 4.9 \times 10^{-6}$; difference to *Net*^{cre} = 35.8% ± 19.0%, Tukey's test, $p = 6.2 \times 10^{-6}$; difference to PRS×8 = 32.1% ± 16.5%, $p = 3.1 \times 10^{-5}$). No significant differences were found between *Dbh*^{cre}, *Net*^{cre}, and PRS×8 mediated transgene expression.

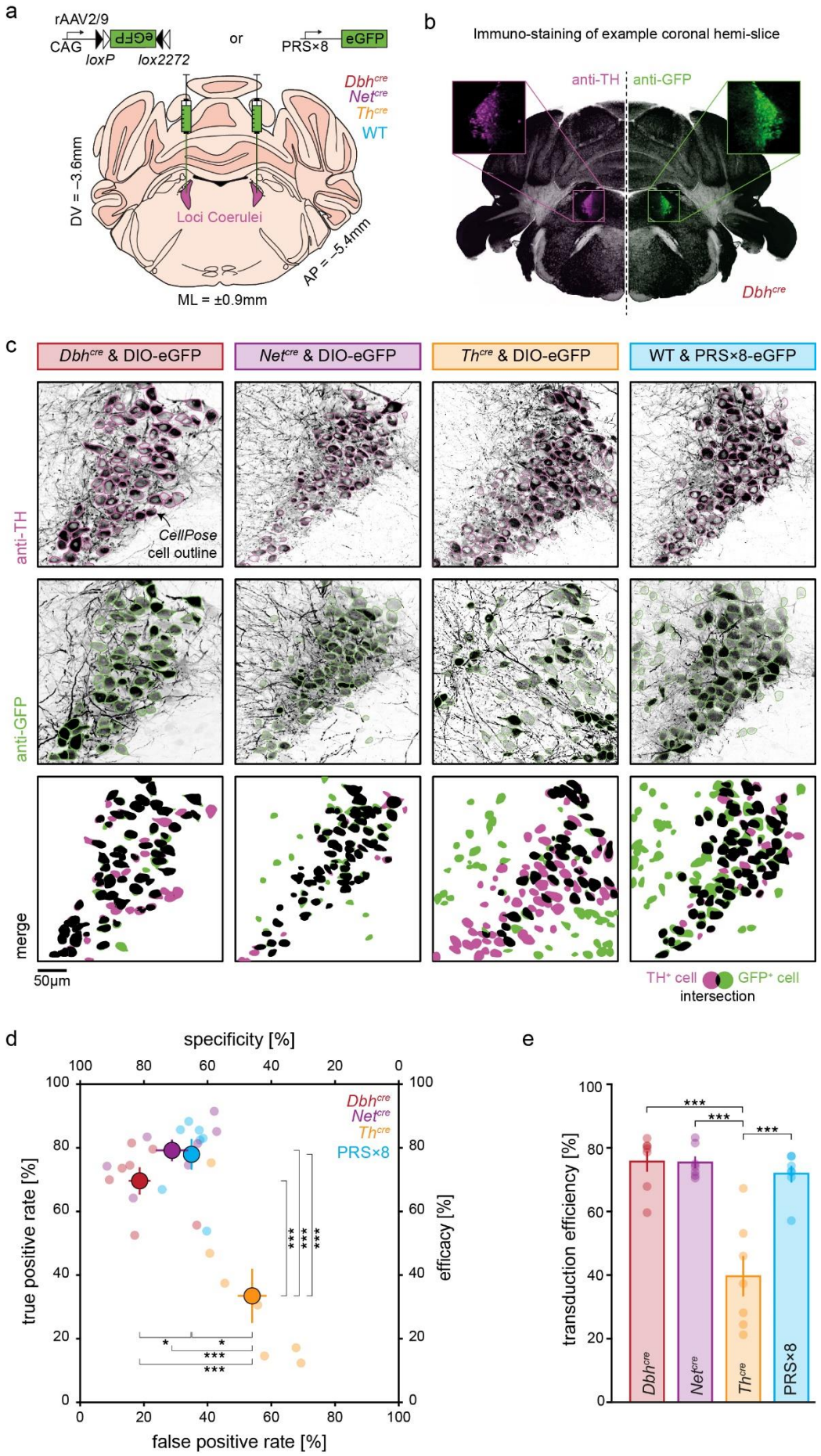
a
rAAV2/9
CAG
eGFP
loxP
lox2272
or
PRS×8
eGFP
Dbhcre
Netcre
Thcre
WT
DV = −3.6mm
Loci Coerulei
AP = −5.4mm
ML = ±0.9mm
b
Immuno-staining of example coronal hemi-slice
anti-TH
anti-GFP
Dbhcre
c
Dbhcre & DIO-eGFP
Netcre & DIO-eGFP
Thcre & DIO-eGFP
WT & PRS×8-eGFP
anti-TH
anti-GFP
merge
CellPose
cell outline
50µm
TH+ cell
GFP+ cell
intersection
d
specificity [%]
true positive rate [%]
efficacy [%]
false positive rate [%]
Dbhcre
Netcre
Thcre
PRS×8
e
transduction efficiency [%]
Dbhcre
Netcre
Thcre
PRS×8

Figure 1 | Viral transduction of LC-NE neurons in different model systems. a, Either CAG-DIO-eGFP (in *Dbh*^{cre}, *Net*^{cre}, and *Th*^{cre}) or PRS×8-eGFP (in WT) was bilaterally injected into the LC of mice (n = 7 animals in each group). Coronal brain slice image from [34] **b**, Example LC hemi-brain slice (vertically mirrored) from a *Dbh*^{cre} animal. Noradrenergic neurons were identified by immunostaining against TH (left, magenta), while transgene expression was visualized with an anti-GFP staining (right, green). **c**, Example LC cells in each of the four model systems (columns) immuno-stained against TH (first row, magenta outlines) and GFP (second row, green outlines). Cells were identified with *CellPose* and boundaries are denoted with colored outlines. Resulting cell masks were then overlaid (third row), and each TH$^+$ cell was labeled as GFP$^+$ (successful transduction, black) when cell masks overlapped 50% or more the size of the TH$^+$ cell, or GFP$^-$ otherwise (missed transduction, magenta). GFP$^+$ and TH$^-$ (erroneous transduction, green) was counted as unspecific transduction. **d**, From cell counts, two quantities were computed for each model system: on the one hand, the true positive rate (y-axis) is computed as N(GFP$^+$|TH$^+$) / N(TH$^+$) and reflects efficacy of TH$^+$ cell transduction. On the other hand, specificity (the inverse of the false positive rate, x-axis) is computed as N(TH$^+$|GFP$^+$) / N(GFP$^+$) and reflects how specific one approach is in transducing exclusively TH$^+$ cells (while ignoring TH$^-$ cells). **e**, Efficacy and specificity were combined into a single metric summarizing the transduction efficiency. This metric formally corresponds to taking the area under the (1-point) ROC curve (in **d**), that is (specificity + efficacy) / 2. In **d** and **e**, error bars denote the standard error of the mean (with n = 7), while statistical significance is denoted by */**/*** for p < 0.05/0.01/0.001, respectively. Only significant differences are indicated.

Control experiments

We performed a number of controls to validate our results and to rule out potential sources of confounding.

In our analyses, we have chosen an overlap threshold between eGFP$^+$ and TH$^+$ cells of ≥ 50% to define co-expression. To assess the generality of our results, we systematically varied the threshold from 5 to 95% (in 5% increments). Relative differences in both efficacy and specificity were independent of the overlap threshold in this range (Fig. S1).

One factor that may lead to underestimation of transduction efficiency in cre lines is non-specific transgene expression of cre-dependent constructs in cre-negative cells, as previously described[35]. To assess the extent of this effect, we bilaterally injected the same DIO-eGFP virus in the LC of 2 wild-type mice. We could not detect eGFP-expressing cells in these animals, ruling out leaky expression of our viral constructs at the titers used in this study (Fig. S2).

To account for potential segmentation errors, we compared results obtained from *CellPose* with manual cell identification by two independent experimenters (CW and AD) in a subset of slices and found agreement between *CellPose* and experimenter rating, as well as between experimenters (Fig. S3). Of note, the training data for *CellPose* was annotated by a third experimenter (LSE), which eliminated experimenter effects.

To investigate potential effects of the GFP staining used in our experiments, we used a secondary antibody in the red spectrum and directly compared cells detected in the green (native eGFP) and red (GFP-stained) channels in a subset of animals (Fig. S4a). We found that the anti-GFP staining increased the number of cells detected by *CellPose* by 21.5 ± 15.3% (t-test against 0: t_{14} = 4.8, p = 2.8 × 10^{-4}; Fig. S4b), and that the averaged normalized brightness

of stained cells exceeded the one of native eGFP-expressing cells by 55.0 ± 35% (*t*-test against 0: $t_{14} = 6.66$, $p = 1.08 \times 10^{-5}$; Fig. S4c). This change in fluorescence was significantly stronger in the dimmest eGFP-expressing cells, i.e. cells expressing relatively low levels of eGFP (*t*-test against 1: $t_{12} = -11.56$, $p = 1.5 \times 10^{-8;}$ Fig. S4d-e). Unfortunately, it is unclear whether low levels of native eGFP expression are due to low promoter activity or weak viral transduction. If low promoter activity causes low eGFP levels, the transgene should accumulate over time, as even low levels of cre recombinase will eventually recombine all floxed genes. Hence, the GFP staining would compensate for the number of detected cells. In contrast, if low eGFP levels result from differences in viral transduction of individual cells, i.e., directly reflects the number of transgene copies per cell, the GFP staining would inflate the number of detected cells. Of note, the changes in fluorescence and cell detection introduced by the anti-GFP staining apply to all experimental groups in the same way.

Ectopic expression of transgenes

In addition to differences in the specificity of neural transduction within the LC and its immediate surroundings, we also observed ectopic GFP expression in various brain regions more distant from the LC (Fig. 2). Again, we found differences between the different model systems with respect to peri-LC transgene expression. The lowest ectopic expression was found in *Dbh*^{cre} animals, where we observed *GFP* expression only in small numbers of cells in the cerebellum (< 10 neurons, 3/7 animals; Fig. S5a) and in the inferior colliculus (< 10 neurons, 1/7 animals; Fig. 2a). In *Net*^{cre} mice, we found a small number of GFP expressing cells in the cerebellum (~1-10 neurons, 4/7 mice Fig. 2b), and moderate GFP expression in the vestibular nucleus of a single mouse (~10-100 neurons, Fig. S5b). In *Th*^{cre} mice, we found substantial ectopic expression in the lateral parabrachial nucleus (~10-500 neurons, 7/7 mice; Fig. S5c), moderate expression in the inferior colliculus (10-100 neurons, 2/7 mice; Fig. 2c) and central gray (< 100 neurons, 1/7 mice; Fig. S5d) and low expression in the cerebellum (< 10 neurons, 1/7 mice; Fig. S5e). Finally, in PRS×8 animals, we found moderate GFP expression both in the vestibular nucleus (~10-200 neurons, 6/7 animals; Fig. S5d), and in the lateral parabrachial nucleus (~10-100 neurons, 3/7 animals; Fig. 2c).

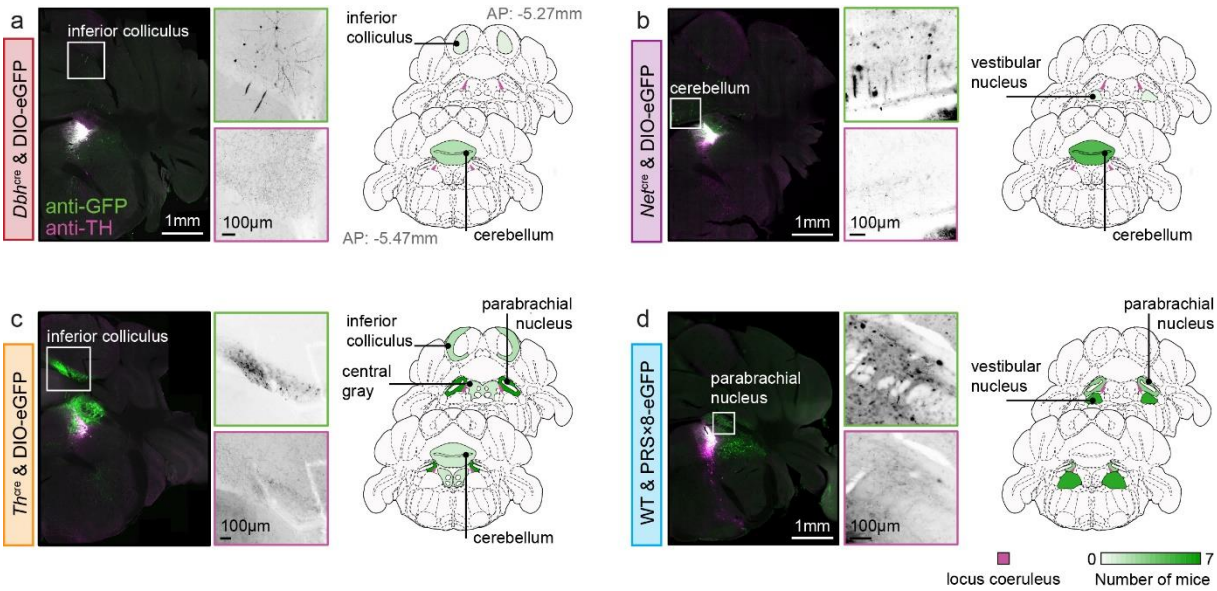

Figure 2 | Ectopic transgene expression across model systems. a-d, On the left panels: example brain slices showing ectopic expression in *Dbh*^{cre}/*Net*^{cre}/*Th*^{cre}/PRS×8 model systems. Immuno-straining against GFP and TH is displayed in green and magenta, respectively. On the right panels: summary of ectopic expression across all mice in *Dbh*^{cre}/*Net*^{cre}/*Th*^{cre}/PRS×8 model systems. Brain regions are color-coded to reflect the number of mice which showed ectopic expression (at least 1 neuron) in the corresponding brain region. Brain slice images from [34].

Success rates of LC targeting

Occasionally, we observed complete absence of the GFP signal (i.e., transgene expression) in one of the two LC of bilaterally injected animals, while expression was strong in the second LC. This pattern of unilateral transgene expression was found in 3/2/1/3 out of each 5 *Dbh*^{cre}/*Net*^{cre}/*Th*^{cre}/PRS×8 mice, respectively (Fig. S6a). In this first set of experiments, we used the same micropipette to inject the viral suspension sequentially in each LC and were concerned that this approach might compromise the success rate of injections (e.g., due to possible inhomogeneous distribution of viral particles in the suspension). Therefore, we added two more mice to each group using a new micropipette for each LC. However, also here, we observed missing transgene expression in some cases with 0/0/2/1 *Dbh*^{cre}/*Net*^{cre}/*Th*^{cre}/PRS×8 regulated mice lacking expression in one of their LC respectively (Fig. S6a). Thus, sequential injection with the same pipette did not explain occasional failure of virus transduction. Importantly, infusion of the viral suspension was also visually confirmed during each injection, and hence the absence of expression in some LC could not be attributed to clogged micropipettes.

Since conditional transgene expression was completely absent in some LC despite ejection of the virus suspension into the intended target area, we aimed to estimate viral spread to test the possibility that LC were missed and nearby brain regions were infused instead. We injected *Dbh*^{cre}, *Net*^{cre}, and *Th*^{cre} mice (n = 3 each) with a so-called 'cre-switch' construct which consists of a double-floxed open reading frame for tdTomato and an inverted open reading frame for eGFP (DO-tdTomato-DIO-eGFP)[36]. Hence, cell type specific expression

of eGFP in cre positive cells allows for characterization of the molecular specificity, while expression of tdTomato in cre negative cells allows for estimation of the general viral spread at the injection site (Fig. S6b). Four weeks after injection, expression of tdTomato in cre negative cells revealed a broad viral spread in most animals, reaching from the midline to the parabrachial nucleus in the mediolateral axis, and from the 4th ventricle to the central gray in the dorsoventral axis (Fig. S6c). Also, in these experiments, we observed 3 animals (out of 9) with only unilateral expression. In these cases, the expression of tdTomato was also absent in the non-expressing hemisphere (Fig. S6c, top-right), suggesting that absence of expression in LC was not due to off-target injection in neighboring brain tissue but rather a failure of virus infection in general.

The overall success rate of injections in our study (80%, 59/74 LC) is in line with previous reports (76-80%)[37,38], which attributed the lack of transgene expression to off-target virus administration (i.e., injection in brain regions adjacent to LC). However, given that our cre-switch experiments have revealed substantial viral spread, we assume that off-target administration into LC-proximal brain tissue would lead to similar viral spread, and, consequently, transgene delivery to the LC. Hence, we suggest instead, that the lack of expression in some LC might result from off-target administration into the 4th ventricle, which is in close proximity to the LC. This might result from minor misalignment on the mediolateral axis during virus injection, resulting in more lateral virus injection in one hemisphere, but virus injection into the 4th ventricle in the other hemisphere. Indeed, when switching the injection coordinates to ±1.1 mm relative to bregma in subsequent experiments, we observed transgene expression in 20/20 LC.

Behavioral screening of cre lines

Unlike the PRS×8 approach, cre-dependent transgene expression relies on the use of mouse lines expressing cre recombinase in a molecularly defined set of cells. As phenotypic alterations have been broadly reported for neuromodulatory cre driver lines[39–41], we screened the driver lines used in this study for behavioral alterations. We applied a series of well-established behavioral paradigms to quantify spontaneous locomotion, anxiety, exploratory behavior, working memory, and spatial learning and memory.

As LC-NE activation is strongly linked to stress and anxiety[42,43], we first compared anxiety-like behavior in cre-expressing *Dbh^{cre}*, *Net^{cre}*, and *Th^{cre}* mice to their wild-type littermates. To this end, mice were left to freely explore an open field arena for 20 minutes (Fig. 3a, left)[44]. As mice show the intrinsic tendency to avoid open areas, the time spent near the walls of the arena serves as a proxy for anxiety, with less anxious mice spending more time in the center. While not all groups displayed significant avoidance of the arena center (p = 0.004/0.06/4×10^{-4}/4×10^{-5}/0.14/6×10^{-5} for *Dbh*^{cre}/*Dbh*^{WT}/*Net*^{cre}/*Net*^{WT}/*Th*^{cre}/*Th*^{WT}, respectively; one-sample t-test against chance level (16 %), n = 16 mice per group), anxiogenic conditions of the paradigm could be confirmed when pooling the data of all mice (p = 6×10^{-15},

n = 96 mice). When comparing 8 males and 8 females of each heterozygous cre-expressing line with a corresponding number of wild-type littermates of each mouse line, we did not detect any significant behavioral difference that could be explained by either genotype, sex, or the interactions of these two factors in any mouse line (Fig. 3a, right; two-way ANOVA; genotype effects: *scie*.45, $p = 0.51$; Net^{cre}: $F_{28} = 0.54$, $p = 0.47$; Th^{cre}: $F_{28} = 0.01$, $p = 0.91$; effects of sex and interactions of sex and genotype are shown in Supplementary table S2). Also, additional readouts used to approximate anxiety and spontaneous locomotion did not indicate any genotype-dependent behavioral difference in any mouse line (Fig. S7).

As an additional experiment approximating anxiety-related behavior, mice were left to explore an elevated plus maze (EPM)[45] for 5 minutes. The EPM consists of four arms radiating from a central platform, with two opposing arms being walled and the other two arms being open (Fig. 3b, left). Thus, mice need to balance their natural exploratory drive with the need to avoid exposed areas. At the start of the experiment, mice are placed on the central platform, and the time spent in the open and closed arms serves as a proxy for anxiety, with less anxious mice spending more time in the open arms. Again, significant avoidance of the open arms could not be demonstrated in each experimental group ($p = 0.08/0.002/5\times10^{-4}/1\times10^{-4}/0.01/0.23$ for $Dbh^{cre}/Dbh^{WT}/Net^{cre}/Net^{WT}/Th^{cre}/Th^{WT}$, respectively; one-sample t-test against chance level (48 %), n = 16 mice per group), but the anxiogenic nature of this paradigm could be validated when pooling the data of all mice ($p = 3\times10^{-12}$, n = 96 mice). Also, in the EPM, we did not detect any behavioral difference that could be explained by either genotype, sex, or the interactions of these two factors in any mouse line (Fig. 3b, right; two-way ANOVA; genotype effects: Dbh^{cre}: $F_{28} = 1.96$, $p = 0.17$; Net^{cre}: $F_{28} = 0.01$, $p = 0.93$; Th^{cre}: $F_{28} = 0.32$, $p = 0.57$; effects of sex and interactions of sex and genotype are shown in Supplementary table S2). Similarly, no behavioral alterations were found in any additional parameters extracted from the EPM (Fig. S8). In conclusion, we did not detect any genotype-related changes in anxiety-like behavior in any mouse line tested in two distinct experimental paradigms under light anxiogenic conditions.

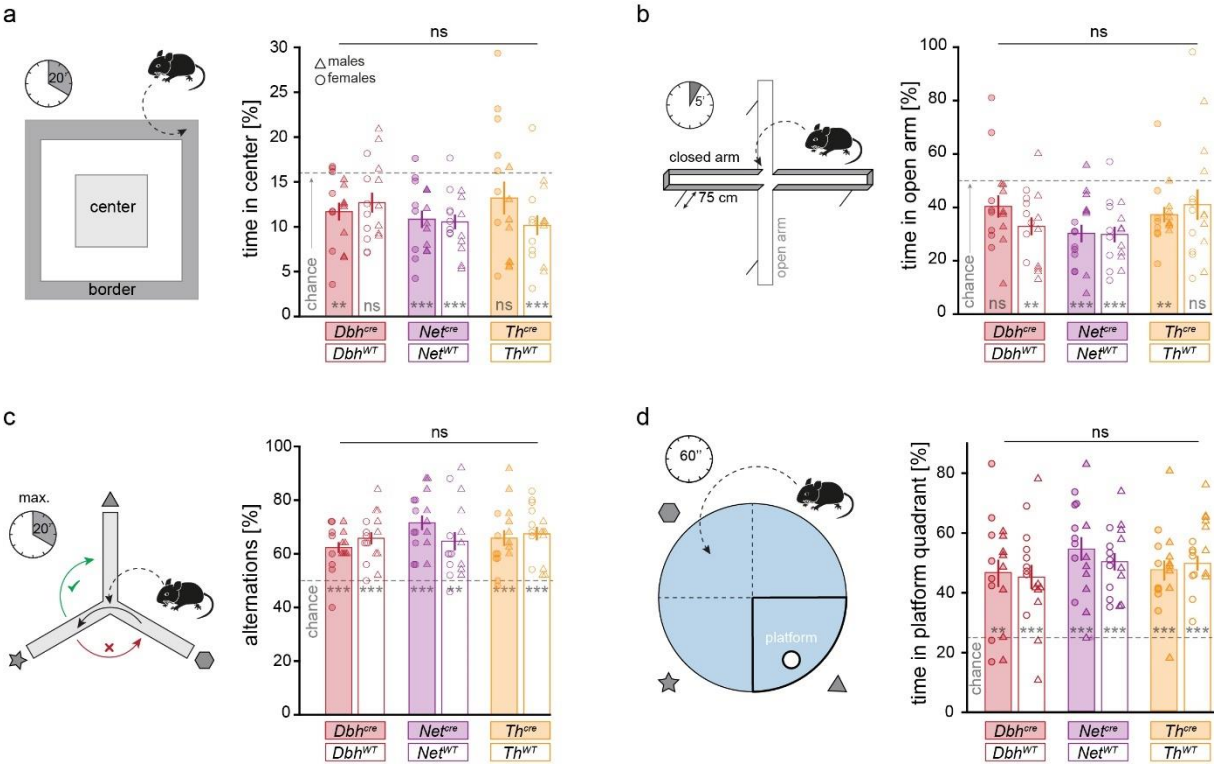

Figure 3 | Behavioral screening of cre-expressing mice. a, left: Mice were placed in one corner of the arena and left to explore the open field arena for 20 minutes. The time spent in the center of the arena approximates anxiety-like behavior. Right: The percentage of time spent in the center of the arena indicates no difference in anxiety-like behavior of cre-expressing mice (filled bars) as compared to wild-type littermates (empty bars) of different driver lines. **b**, left: Mice were placed on the central platform of the elevated plus maze and left to explore the maze for 5 minutes. The time spent in open arms of the maze approximates anxiety-like behavior. Right: The percentage of time spent in open arms indicates no difference in anxiety-like behavior of cre-expressing mice as compared to wild-type littermates in any driver line. **c**, left: Mice were placed in the center of the Y-maze and left to explore the maze until 26 transitions were made, for a maximum of 15 minutes. Upon the first transition between arms (black arrow), the next transition is expected to occur towards the previously unexplored arm (green arrow), rather than to the arm that was just visited before (red arrow). Right: The percentage of alterations (i.e., consecutive visits of all three arms) over the total number of transitions is above chance level (dashed line) in all groups, while no genotype-dependent differences in working memory were detected between cre-expressing mice and wild-type littermates in any mouse line. **d**, left: Mice are trained to find a hidden platform in a circular pool filled with opaque water on two consecutive days. On day three, the platform is removed, and the time spent in the area where the platform was previously located serves as a proxy for spatial memory. Right: the percentage of time spent in the platform quadrant was above chance level (dashed line) in all groups, while no genotype-dependent differences in spatial memory were detected between cre-expressing mice and wild-type littermates in any mouse line. All data is depicted as mean ± standard error of the mean. ns = not significant. **/*** for $p < 0.01/0.001$, respectively, tested against chance level. n = 8 females (circles) and 8 males (triangles).

Recent studies have demonstrated the involvement of the LC-NE system in the formation of episodic and spatial memory[46,47], which we investigated in two additional experiments. First, we employed the Y-maze paradigm to approximate working memory in mice. In this assay, mice are placed in a maze with 3 symmetrically radiating arms, which they are free to explore. Based on the innate tendency to explore novel environments, mice spontaneously alternate between arms, i.e. when leaving one arm, they tend to move to the

arm that was not previously visited, rather than the arm that was previously explored (Fig. 3c, left; visual cues were given to distinguish the different arms)[48,49]. This was quantified as the fraction of alternations (i.e., consecutive visits of all three arms) over the total number of transitions. The fraction of alternations was above chance level in all groups ($p < 0.01$; Bonferroni-corrected one-sample *t*-test), indicating intact working memory in all groups. No genotype-related behavioral changes were found (Fig. 3c, right; two-way ANOVA; genotype effects: Dbh^{cre}: $F_{28} = 1.23$, $p = 0.26$; Net^{cre}: $F_{28} = 2.48$, $p = 0.13$; Th^{cre}: $F_{28} = 0.23$, $p = 0.63$; effects of sex and interactions of sex and genotype are shown in Supplementary table S2, additional results from Y-maze experiments are shown in Fig. S9).

Finally, to investigate spatial memory formation, we performed the Morris Water Maze (MWM) task[50]. In the MWM, mice are placed in a circular pool filled with opaque water that contains a hidden platform placed just below to the surface that mice can access to escape the water (Fig. 3d, left; visual cues for spatial orientation were placed around the pool). The MWM task was performed on three consecutive days after habituating mice to the water. On the first two days, each mouse was placed in the water four times, at pseudo-randomized positions in each trial. Decreased latencies and travel distances to reach the platform during these training sessions indicated successful spatial learning in all experimental groups (Fig. S10). On the second day, after the first two training trials, a probe trial was performed, in which the platform was removed. The time spent in the platform quadrant approximates short-term memory. On day three, a single probe trial was done, from which long-term memory can be measured. The time spent in the platform quadrant during the probe trial on day 3 was above chance level in all groups ($p < 0.01$; Bonferroni-corrected one-sample *t*-test), indicating intact spatial memory formation. No genotype-dependent behavioral changes were found (Fig. 3d, right; two-way ANOVA; genotype effects: Dbh^{cre}: $F_{28} = 1.14$, $p = 0.29$; Net^{cre}: $F_{28} = 0.56$, $p = 0.46$; Th^{cre}: $F_{28} = 0.34$, $p = 0.56$; effects of sex and interactions of sex and genotype, as well as results of the short-term memory test on day two are shown in Supplementary table S2, additional results of the MWM experiments on day 3 are shown in Fig. S11). In conclusion, we found no genotype-related behavioral differences between cre-expressing mice and wild-type littermates in Dbh^{cre}, Net^{cre}, or Th^{cre} mice in the four behavioral assays considered.

PRS×8-based constructs for monitoring LC activity

Transgene expression driven by the PRS×8 promoter, which has high efficacy and good local specificity (Fig. 1), is independent of cre recombinase. Thus, molecular targeting of LC-NE neurons with the PRS×8 promoter can be applied either to wild-type mice, eliminating the need for a cre driver line, or to a different cre driver line, providing access to two genetically distinct neuronal populations in the same animal. In addition, PRS×8-based transgene expression can be applied to different species, as demonstrated in rats[23,26,51,52]. As there are

currently very few PRS×8-based constructs available, we developed a set of PRS×8-based constructs to enable the monitoring and control of LC-NE activity.

To optically monitor LC-NE activity in the green and red spectrum, we developed two constructs encoding either jGCaMP8m[53] or jRGECO1a[54] under the control of the PRS×8 promoter. After injection of rAAV2/9-PRS×8-jGCaMP8m and implantation of an optical fiber above the LC of a wild-type mouse, we obtained awake, head-fixed fiber photometry recordings (Fig. 4a-c). Since the LC-NE system causally controls pupil-linked arousal[55], we simultaneously monitored the animal's pupil diameter, which we aligned to peaks of LC activity as inferred from the photometry recordings. As expected, peaks in LC activity were followed by periods of pupil dilation, confirming a biologically relevant signal obtained from PRSx8-mediated jGCaMP8m expressing LC-NE neurons (Fig 4b). Similarly, we were able to record fiber photometry signals from LC-NE neurons in the red spectrum after viral transduction of the rAAV2/9-PRS×8-jRGECO1a (Fig. 4d-f). As previously reported in a comparison between jRGEGO1a and GCaMP6s[54], we observed stronger bleaching in recordings performed with jRGECO1a as compared to jGCaMP8m (Fig. S12).

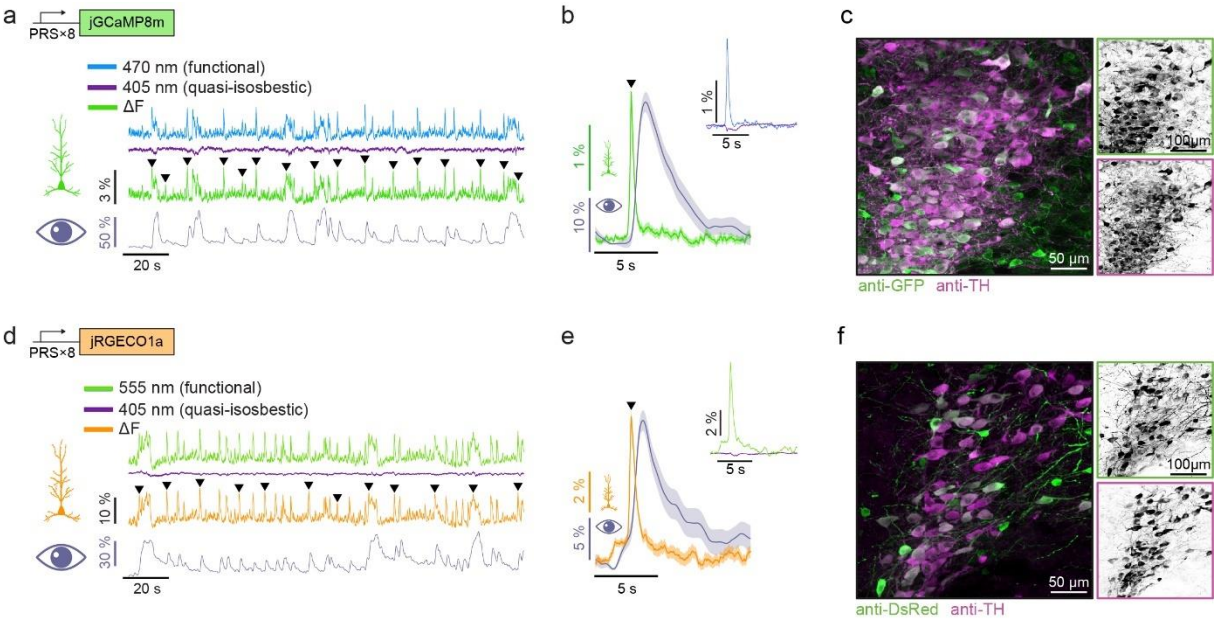

Figure 4 | PRSx8-mediated constructs to monitor LC activity. a, Exemplary traces (3 minutes) of bleaching-corrected jGCaMP8m fluorescence when excited at 470/10 nm (blue) and 405/10 nm (purple), ΔF (green), and pupil diameter (gray). Detected peaks in the ΔF trace — with a minimum inter-peak interval of 10 s to allow for pupil dilations to return to baseline — are indicated by arrowheads. **b,** ΔF (green, mean ± standard error of the mean) and pupil diameter (gray) locked to ΔF peaks (arrowhead; *n* = 121 peaks from a recording of ~30 minutes duration). Inset: Peak-aligned fluorescence upon excitation at 470/10 nm (blue) and 405/10 nm (purple) confirms the calcium-dependence of recorded signals. **c,** Immuno-staining against GFP to visualize jGCaMP8m (green) and TH to visualize noradrenergic neurons of the LC (magenta). **d,** Exemplary traces (3 minutes) of bleaching-corrected jRGECO1a fluorescence when excited at 562.5/15 nm (green) and 405/10 nm (purple), ΔF (orange), and pupil diameter (gray). Detected peaks in the ΔF trace are indicated by arrowheads. **e,** ΔF (orange) and pupil diameter (gray) locked to ΔF peaks (arrowhead; *n* = 67 peaks from a recording of ~20 minutes duration). Inset: Peak-aligned fluorescence upon excitation at 562.5/15 nm (green) and 405/10 nm (purple) confirms the calcium-dependence of

recorded signals. **f,** Immuno-staining against DsRed to visualize jRGECO1a (green) and TH to visualize noradrenergic neurons of the LC (magenta).

Discussion

The LC-NE system consists of a small number of neurons located deep in the brain stem. It is responsible for the modulation of a wide range of body and brain functions. In recent years, an increasing number of studies have used genetic strategies to selectively and specifically target the LC-NE system. Obviously, the interpretation of these studies strongly depends on the reliability of transgene expression in this small cell population. However, a direct quantification of these parameters is not always reported, and a direct comparison of these model systems is lacking. In this study, we performed a side-by-side comparison of four strategies for viral-based genetic manipulation of the mouse LC, encompassing LC transduction with floxed transgenes in *Dbh*^{cre}, *Net*^{cre} and *Th*^{cre} transgenic driver lines, and transgene expression under the control of a synthetic, NE-specific promoter (PRS×8).

Using immunohistological analysis, we found differences in both expression efficacy and specificity between these model systems. *Dbh*^{cre} mice and *Net*^{cre} *mice* showed the highest specificity and efficacy of transgene expression, with no significant differences between them. In comparison, PRS×8 promoter-driven expression showed comparable efficacy to *Dbh*^{cre} *and Net*^{cre} mice, but lower specificity compared to *Dbh*^{cre} mice. Conditional expression in *Th*^{cre} mice – a line, which is commonly used to target LC – showed both lower efficacy and specificity than the other approaches. Finally, substantial ectopic transgene expression in regions distant from the LC was observed, particularly with PRS×8- and *Th*^{cre}-mediated transgene expression.

It is important to note that TH-positive neurons have been reported in brain areas close to the LC, such as the parabrachial nucleus[63]. Although the ectopic expression in our study was not localized to these TH-positive neurons (as indicated by the absent TH co-staining), this population should be kept in mind as it may lead to erroneous interpretations of the function of LC-NE neurons if LC-specificity is taken for granted in *Th*^{cre} mice. Ectopic transgene expression was much less pronounced in *Net*^{cre} mice, and only very low ectopic expression was observed in *Dbh*^{cre} mice. In fiber photometry experiments that directly target the LC, ectopic expression may be less of a concern because signals are typically recorded in close proximity to the tip of the optical fiber[64,65], adding spatial precision to the molecular specificity of transgene expression. By contrast, recordings in putative projection sites may get contaminated by afferents from ectopically expressing neurons. In addition, in optogenetic studies, where the intensity of activation light is typically chosen to be well above threshold, light scattering could also lead to the activation of opsins ectopically expressed in tissue distant the fiber tip.

As mentioned above, a direct side-by-side comparison of virus-mediated LC transduction under comparable conditions (i.e., same viral titers, injection volumes, viral serotypes, etc.) has not yet been performed. However, several different studies reported the

transduction efficiency and specificity individually for a given model system. In *Dbh*^{cre} mice, viral transduction efficacies between 83% and 96% of *TH*-immunoreactive neurons have been reported[66–68], with a specificity of 95%[67]. In *Net*^{cre} mice, an efficacy of ~99% was reported, with no transgene expressing cells found outside of the LC[19]. However, it is important to note that transgene expression in this study was not achieved by viral injections but by crossing *Net*^{cre} mice with a reporter mouse line. Using transgene expression mediated by the PRS×8 promoter, an efficacy of 83% of TH^{+} neurons[26] at a specificity of 97-100%[23,26,52] was reported in rats. In mice, a specificity of 95-98% was described for PRS×8 promoter-mediated expression, while efficacy was not quantified[24,25]. In addition, a more recent study by Stevens et al.[38] reported efficacies ranging from ~50 to 90%, with specificities between ~60 and 95% (depending on the volume and titer of the injected virus). This study reported the best results with a titer of 1×10^{11} gc/ml (71-77% efficacy, ~96% specificity). At higher titers (1×10^{12} gc/ml), specificity decreased to 60%. At even higher titers ($5\text{-}20 \times 10^{12}$ gc/ml) the efficacy also decreased, and substantial toxicity was observed. The titer used in our study (8×10^{11} gc/ml) comes closest to the 1×10^{12} gc/ml condition of Stevens et al., and comparable efficacy (70-90%) and specificity (60-80%) were observed. Therefore, it is likely that the specificity of PRS×8 driven expression can be improved in the future by using lower titers. However, it is important to note that the majority of studies used PRS×8-driven constructs in combination with recombinant adenoviruses[23] or canine adenovirus 2 (CAV-2)[24–26,38], which have a different tropism and transduction efficacy than rAAV2/9 used in our study[69]. Considering rAAV pseudotypes, insufficient PRS×8-mediated transgene expression was reported with rAAV2/7[70] (~20.6 % efficacy), whereas robust expression was reported after injection of rAAV2/9[37,52]. These findings highlight the importance of viral serotype and careful titration of the viral titer when implementing the PRS×8 promoter for genetic manipulation of the LC.

In *Th*^{cre} mice, we show that cre-mediated expression only partially covers TH-positive LC neurons. Low efficacy and ectopic, cre-dependent transgene expression were also previously described in close proximity to the LC[20,71], the substantia nigra[20], the VTA[72,73], and various brain regions not directly related to catecholaminergic signaling[21,73,74]. A detailed study by Lammel and colleagues[73] reported specificities of 48 and 59% in the ventral tegmental area of *Th*$^{IRES\text{-}cre}$ and *Th*^{cre} mice, respectively, which aligns well with the specificity we observed in the LC. Higher efficacy and specificity for *Dbh*^{cre} when compared to *Th*^{cre} mice was also reported for catecholaminergic neurons in the A1/C1 area of the brainstem, but differences were not as pronounced as in our study[75]. Overall, our results are consistent with previous findings from various different studies investigating cre-dependent expression in the LC. Thus, our systematic comparison reveals directly the marked differences in expression patterns among the different cre driver lines upon viral transduction or PRS×8 mediated transgene expression.

The observed differences in transgene expression patterns may be explained, at least in part, by the different strategies used to generate different mouse lines: *Dbh*^{cre} mice were generated using a knock-in/knock-out strategy, resulting in cre expression directly from

the *Dbh* locus. While this approach disrupts endogenous *Dbh* expression, the use of heterozygous *Dbh*^{cre} mice allows for safe and specific cre expression with a low risk for unwanted side effects. In contrast, the transgenic *Th*^{cre} mice were generated by random insertion of a construct containing the *Th* promoter followed by a cre coding sequence. This could explain leaky cre expression due to potential activity of other promoter elements in the vicinity of the integration site. However, also different strategies for *Th*-specific cre-expression yielded low specificity in the VTA – as shown for knock-in mice expressing Cre-recombinase from the downstream-untranslated region of the endogenous Th gene via an internal ribosomal entry sequence (IRES)[73]. The *Net*^{cre} mice (and other commonly used *Dbh*^{cre} and *Th*^{cre} lines[16]) are bacterial artificial chromosome (BAC) transgenic mice generated by random insertion of a BAC sequence containing the gene of interest and a cre coding sequence. The inclusion of the gene increases the possibility of preserving key regulatory elements required for accurate cell-type-specific expression, which are not included in the case of *Th*^{cre} mice or when using the synthetic, minimal PRS×8 promoter. However, it is important to note that regulatory elements are often distant from the promoter, and therefore incomplete and ectopic transgene expression similar to traditional transgenic mice may also be found in BAC transgenic mice[16]. Unpredictable ectopic expression may also be driven by transcriptional regulatory elements of genes flanking the transgene insertion site. In addition, random transgene insertion may interrupt endogenous genes, resulting in loss-of-function mutations and unexpected phenotypes. These effects are avoided in targeted knock-in alleles, as was used to generated the *Dbh*^{cre} mice. It is important to mention that additional *Th*^{cre} and *Dbh*^{cre} mouse lines exist that have also been generated using BACs[16] and targeted mutations[21]. However, the use of these mice is much less widespread and there are currently no vendors maintaining colonies of these lines.

Ectopic expression is not limited to the *Th* promoter, but has also been reported in a wide variety of model systems, including cholinergic and catecholaminergic cells of the retina[76,77], dopaminergic cells of the dorsal raphe nucleus[78] and the limbic system[79], and somatostatin-expressing interneurons[80] and microglia[81] in the cerebral cortex. Such ectopic expression may result from promoters that are weakly active, leading to low levels of native protein expression, which may not be functionally relevant. Similarly, low expression levels of a direct reporter, such as a fluorophore in a reporter mouse line, may not be a major concern because the detected signal may be much weaker compared to true positive cells exhibiting high activity of the promoter of interest. However, in cre-reporter line, even low levels of cre are sufficient to recombine floxed transgenes over time, leading to substantial expression of the transgene and thus uncoupling of endogenous cre expression levels from cre-dependent transgene expression[82,83]. This explanation is consistent with reports from homozygous Ai32 reporter mice where immunostainings revealed leaky channelrhodopsin-2 expression throughout the brain in the absence of cre, but at levels insufficient to induce detectable photocurrents[84]. Other explanations for ectopic expression include legitimate but transient promoter expression during development[21,28,29,73,83], changes in endogenous expression

patterns resulting from transgene integration itself[76], or recombination of cre in the germline[83].

Phenotypic alterations have been previously reported for different cre driver lines to access the cholinergic (*Chat*^{cre})[39] and dopaminergic systems (*Dat*^{cre}, *Dat*^{IREScre}, and *Th*^{cre} upon amphetamine application)[40,41]. Therefore, we performed a behavioral screening sensitive to anxiety-like behaviors as well as learning and memory, all of which have been linked to LC function. We found no genotype-related effect on spontaneous locomotion, anxiety, exploratory behavior, working memory, and spatial learning and memory. These results are particularly relevant for the *Dbh*^{cre} line, because the knock-in/knock-out design of this mouse line disrupts endogenous *Dbh* expression in one allele of heterozygous animals. This approach could lead to reduced levels of norepinephrine while accumulating its precursor molecule dopamine, and consequently disrupting behavior. Furthermore, we did not observe any sex-related effects on anxiety-like behavior, which is in contrast to a recent study reporting higher levels of anxiety in female mice using the open field and elevated plus maze paradigms[85]. While sex differences in the EPM were confirmed by one additional study[86], two studies reported the absence of sex effects on anxiety-like behavior using the open field test[86,87]. These discrepancies may be explained (in part) by the estrous cycle, which is linked to *Th* transcription[88]. It has been demonstrated that mice in the proestrus and estrus stages showed increased anxiogenic behavior, while mice in other stages were comparable to males[85]. As the stage of the estrous cycle was not controlled in our experiments, experimental groups randomly composed of females in different estrous cycles may have masked sex-dependent effects in our experiments. Further factors that have been shown to influence the outcome of these experimental paradigms are the sex of the experimenter[89,90], the history of handling[91,92], as well as non-explicit factors of the laboratory itself[93,94]. In conclusion, our results suggest that all mouse lines investigated here can be used equally, at least for the behavioral assays we have included. However, caution should be exercised when extrapolating these results to other experimental paradigms such as instructed behavior or experimental conditions that differ substantially from those we used.

We show that *Dbh*^{cre}, *Net*^{cre}, and PRS×8-mediated transgene expression provides reliable access to the LC-NE system. In parallel, we did not observe any genotype-related behavioral changes in any mouse line. Apart from these aspects, additional factors should be considered when deciding which LC-targeting strategy to use. First of all, *Dbh*^{cre} and *Net*^{cre} mice showed the highest specificity. Second, the cre-lox system is widely established. Therefore, cre driver lines can be easily combined with off-the-shelf viral constructs that are readily available from public commercial and non-commercial repositories. Finally, driver lines can be crossed with various reporter lines, allowing reproducible transgene expression without the need for stereotactic surgery. Of note, *Dbh*^{cre} mice are commercially available in public repositories, making them available to the scientific community, while a material transfer agreement is required to obtain *Net*^{cre} mice. In contrast, PRS×8-based transgene expression is possible in wild-type mice and, therefore, no transgenic mouse line colonies are

required. This not only eliminates the risk of mouse-line-dependent phenotypic effects that we may have missed, but also facilitates easy and straightforward access to the LC-NE system. Moreover, it reduces the number of excess animals that can result from unwanted genotypes when breeding a particular mouse line. In addition, PRS×8 allows a high degree of flexibility for manipulation and readout of different molecularly defined circuits when combined with cre lines other than those related to the noradrenergic system. Finally, the PRS×8-system can be implemented in species other than the mouse, where driver lines are not commonly available, as recently demonstrated in the rat[26]. In this species, the only alternative driver line is a *Th*^{cre} line (which, in contrast to the mouse, has been reported to be reliable in terms of both efficacy and specificity)[22,95]. However, regardless of the model system chosen, our study highlights the importance of rigorous post-mortem verification of viral transduction and the implementation of appropriate controls for each system.

Caution should be exercised in extrapolating our conclusions to different experimental settings. First, we relied on a single viral titer in all model systems. While all experimental groups were injected with the same amount of virus, it has been shown that the efficacy, specificity, and potential toxicity of PRS×8-mediated gene expression are highly dependent on the viral titer[38]. Similarly, the specificity of cre-dependent transgene expression is dependent on the viral titer[96,97]. Therefore, it may well be that greater efficacy and specificity of gene expression can be achieved when optimizing the viral titer for a specific application. In addition, all our experiments were performed with rAAV2/9, and, therefore, may not be generalizable to different serotypes or even different virus families. For example, an rAAV pseudotype with less broad tropism than rAAV2/9 may lead to reduced ectopic expression and, therefore, higher apparent specificity. Conversely, lower efficacy may be observed, if viral transduction of noradrenergic neurons is limited. Another consideration relates to the choice of antibodies for the detection of transgene expression and cell identity. For example, we have broadly stained against tyrosine hydroxylase while anti-DBH or anti-NET antibodies could have been used to exclusively detect noradrenergic neurons. However, it has been shown that immunostaining against DBH[98] and against NET[99] overlaps almost perfectly with staining against TH in the LC, justifying the choice of the antibody used in our LC-focused study. Notably, all of our experimental groups were stained with the same antibody, and the outcome of our study did not favor the *Th*^{cre} line.

In conclusion, we present a quantitative side-by-side comparison of four different strategies to genetically access the mouse LC, resulting in heterogeneous patterns of transgene expression. These findings may help in the design of future studies and in the interpretation of results obtained in previous studies using any of these model systems. For example, a recent study described micro-arousals, but no sustained wake episodes upon optogenetic LC activation in *Dbh*^{cre} mice, whereas sustained wake episodes were evoked by optogenetic LC activation in *Th*^{cre} mice[71]. This discrepancy may be due to the different neuronal populations targeted in each line and highlights the importance of selecting an appropriate model system. In addition to the analysis of transgene expression patterns, we

have developed AAV-based tools relying on the PRS×8 promoter for marking LC neurons and monitoring LC activity in both the green and red spectra, increasing experimental flexibility and facilitating the investigation of the LC-NE system in various genetic backgrounds. Taken together, these results contribute to the design of more refined studies and thus to a deeper understanding of the heterogeneous functionality of the LC-NE system in the future.

Material and Methods

Animals. Experiments were performed on adult (2-6 months of age) C57BL/6J, *Th*^{cre}[20], *Net*^{cre}[19] and *Dbh*^{cre}[17] mice, housed in cages with nesting material with no more than 5 animals per cage at the animal facility of the *Center for Molecular Neurobiology* of the *University Medical Center Hamburg-Eppendorf* or at the *Medical Faculty Mannheim of the University of Heidelberg*. Animals were kept in a 12/12 h light/dark cycle, at 20-24°C and 40-65% humidity, and access to water and food ad libitum. All experiments were performed in compliance with German law according to the directive 2010/63/EU of the *European Parliament* on the protection of animals used for scientific purposes. Protocols were approved by the *Behörde für Gesundheit und Verbraucherschutz* of the city of Hamburg and the *Regierungspräsidium Karlsruhe*, respectively.

Molecular biology. The double-floxed inverted open reading frame variant for cre dependent expression of *eGFP*[59] was created by cloning *eGFP* in antisense direction, flanked by two loxP and lox2272 sites, behind the CAG promoter into an AAV2 backbone. PRS×8-based constructs were created by cloning the respective transgene behind 8 repetitions of a de novo synthetized Phox2a/Phox2b response site (PRS; based on the only PRS×8 construct (#89539) available from *AddGene* at the time this study started) into an AAV2 backbone. PRS×8 constructs were generated for the expression of the green light emitting reporter protein *eGFP*[59] (pAAV-PRS×8-eGFP; *AddGene* #192589), the green light emitting calcium indicator jGCaMP8m[53] (pAAV-PRS×8-jGCaMP8m; *AddGene* #210400) and the red light emitting calcium indicator jRGECO1a[54] (pAAV-PRS×8-jRGECO1a; *AddGene* #210399). DNA was then packed into recombinant adeno-associated virus serotype 2/9 (rAAV2/9) at the vector core facility of the *University Medical Center Hamburg-Eppendorf*, Germany.

Stereotactic injections and fiber implantation. For surgical procedures, mice were either anesthetized with Midazolam/Medetomidine/Fentanyl (MMF; 5/0.5/0.05 mg/kg bodyweight in NaCl, intraperitoneal), or with Isoflurane (5% for induction, ~1.5% for maintenance). In the case of isoflurane anesthesia, adequate analgesia was achieved with buprenorphine (0.1 mg/kg in NaCl, intraperitoneal). After confirming anesthesia and analgesia by the absence of the paw withdrawal reflex, the head was shaved with a fine trimmer and sterilized with iodine (*MundiPharma*). Mice were then fixed with an auxiliary ear bar (EB-6, *Narishige Scientific*) in a stereotactic frame and positioned on a heating blanket to maintain body temperature. Eyes were covered with an eye ointment (*Vidisic*, *Bausch + Lomb*) to avoid drying. Subsequently, the scalp was opened (~1 cm incision) and the skull was cleaned with

NaCl (0.9%; *Braun*) and a bone scraper (*Fine Science Tools*). Bregma and lambda were identified and stereotactically aligned. A small craniotomy was then performed above the locus coeruleus (AP: –5.4; ML: ±0.9; DV: –3.6 mm relative to bregma) using a dental drill (*Foredom*), and was constantly kept moist to prevent drying.

The viral suspension was drawn into a borosilicate glass pipette (pulled from 0.2 mm glass capillaries with a PC-100 puller; *Narishige*) using negative air pressure. 300 nl of titer-matched (8×10^{11} gc/ml) viral suspension containing rAAV2/9 carrying DNA encoding *eGFP* either in a cre-dependent (double-floxed inverted reading-frame, DIO) manner under control of the CAG promoter (in the case of Dbh^{cre}, Net^{cre} and Th^{cre} animals) or unconditional under control of the PRS×8 promoter (in the case of C57BL/6J mice) were bilaterally injected into the LC with an injection speed of ~100 nl/min using a custom-made, air-pressure driven injection system for the analysis of transgene expression in the different model systems. Injections of rAAV2/9-Ef1a-DO-DIO-tdTomato-eGFP (2.3×10^{13} gc/ml; *AddGene* plasmid #37120)[36] were performed in Dbh^{cre}, Net^{cre} and Th^{cre} animals to estimate the viral spread. For fiber photometry experiments we injected rAAV2/9-PRS×8-jGCaMP8m (3×10^{13} gc/ml) and rAAV2/9-PRS×8-jRGeco1a (2×10^{13} gc/ml) into wild-type mice. Given that *eGFP* expression was not observed in all injected LC of our transduction experiments, which we attributed to virus injection into the 4th ventricle (see Fig. S6), we injected these constructs at ±1.1 mm relative to bregma on the mediolateral axis. Changing medio-lateral coordinates (from ±0.9 to ±1.1mm) lead to increase in transduction rate from 79.7 % to 100% (n = 59/20 out of 74/20 LC). After virus injection, the glass micropipette was kept in place for at least 5 min to avoid unnecessary viral spread and was then slowly withdrawn. In the case of histological experiments, the skin was closed with simple interrupted sutures and covered with iodine. In the case of fiber photometry experiments, optical fibers (R-FOC-BL400C-50NA: 400 µm diameter, 0.5NA; *RWD*) were inserted at AP: –5.4; ML: ±1.0; DV: –3.5 mm relative to bregma using a stereotactic micromanipulator. Fiber implants, as well as a metal headpost (00-200 500 2110; *Luigs & Neumann*) for animal fixation during the experiment, were fixed to the roughened skull using cyanoacrylate glue (Pattex; Henkel) and dental cement (Super Bond C&B; *Sun Medical*). The incised skin was then glued to the dental cement to close the site, before it was covered with iodine. Mice received analgesia (Carprofen; 4 mg/kg bodyweight, subcutaneous), and Atipamezole/Flumazenil/Buprenorphine (FAB) was administered (2.5/0.5/0.1 mg/kg bodyweight, intraperitoneal) to antagonize anesthesia in the case of MMF; Isoflurane anesthetized mice were simply removed from the Isoflurane. For recovery, mice were placed in a cage which was placed on a heating pad. Meloxicam was mixed with soft food for the following two days.

Tissue collection. For perfusions, mice were deeply anesthetized with Ketamine/Xylazine (180/24 mg/kg bodyweight, intraperitoneal), which was confirmed by the absence of the paw withdrawal reflex. Mice were fixed on a silicone pad and transcardially perfused with ~50 ml of phosphate buffered saline (PBS) to rinse out the blood and subsequently with ~50 ml of 4% paraformaldehyde (PFA; pH 7; *Carl Roth GmbH*) to fix the

tissue. Brains were explanted and post-fixed in 4% PFA for at least 24h. After fixation brains were embedded in 3% agarose (*Genaxxon Bioscience*) and coronal slices of ~50 µm thickness were obtained using a vibratome (VT 1000S, *Leica*). Slices were stored in PBS at 4°C until they were stained and mounted on microscope slides.

Immunohistochemistry. To block unspecific binding sites for antibodies, brain slices were incubated in 10% normal goat serum (NGS) and 0.3-0.5% Triton X-100 in PBS for 2h at room temperature. Slices were then incubated for two days at 4°C in a carrier solution (2% NGS, 0.3-0.5% Triton X-100, in PBS) containing primary antibodies (see below) to allow for sufficient target protein-primary antibody interaction. Subsequently, slices were rinsed 3 times for 5-10min in PBS to remove unbound primary antibodies. Following the washing steps, slices were incubated with secondary antibodies (see below) in the above-mentioned carrier solution over night at 4°C. Washing steps were repeated as described before in order to remove unbound secondary antibodies. Finally, slices were mounted on microscope slides using *Fluoromount* mounting medium (*Serva*, Germany).

To analyze eGFP expression in TH^+ cells of the LC (Fig. 1, Fig. 2, Fig. S2, Fig. S5), slices were incubated with primary antibodies against tyrosine hydroxylase (1:1000; AB152; *Merck Millipore*) derived from rabbit and against green fluorescent protein (1:750; A10262; *Invitrogen*, *Thermo Fisher Scientific*) derived from chicken, while Alexa Fluor 546 goat anti-rabbit (1:1000; A11035; *Invitrogen*, *Thermo Fisher Scientific*) and Alexa Fluor 488 goat anti-chicken (1:1000; A11039; *Invitrogen*, *Thermo Fisher Scientific*) secondary antibodies were used. To analyze the difference of natively expressed eGFP fluorescence and antibody-stained eGFP fluorescence (Fig. S4), slices were incubated with a primary antibody against green fluorescent protein (1:750; A10262; *Invitrogen*, *Thermo Fisher Scientific*) derived from chicken and an Alexa Fluor 546 goat anti-chicken secondary antibody (1:1000; A11040; *Invitrogen, Thermo Fisher Scientific*). In DO-DIO-experiments (Fig. S6), slices were incubated with primary antibodies against tyrosine hydroxylase (1:1000; AB152; *Merck Millipore*) derived from rabbit and against green fluorescent protein (1:750; A10262; *Invitrogen*, *Thermo Fisher Scientific*) derived from chicken, while Alexa Fluor 647 goat anti-rabbit (1:1000; A32733; *Invitrogen*, *Thermo Fisher Scientific*) and Alexa Fluor 488 goat anti-chicken (1:1000; A11039; *Invitrogen*, *Thermo Fisher Scientific*) secondary antibodies were used. No staining was performed against tdTomato. To visualize GCaMP8m in TH^+ neurons of the LC (Fig. 4a), slices were incubated with primary antibodies against tyrosine hydroxylase (1:1000; AB152; *Merck Millipore*) derived from rabbit and against green fluorescent protein (1:500; A10262; *Invitrogen*, *Thermo Fisher Scientific*) derived from chicken, while Alexa Fluor 647 goat anti-rabbit (1:1000; A32733; *Invitrogen*, *Thermo Fisher Scientific*) and Alexa 488 goat anti-chicken (1:1000; A11039; *Invitrogen*, *Thermo Fisher Scientific*) were used as secondary antibodies. To visualize jRGeco1a in TH^+ neurons of the LC (Fig. 4d), slices were incubated with primary antibodies against tyrosine hydroxylase (1:500; Cat. No. 213 104; *Synaptic Systems*) derived from guinea pig and against DsRed (1:500; Cat. No. 632496; *TaKaRa Bio*) derived from rabbit, while Alexa Fluor 647 goat anti-guinea pig (1:200; A21450; *Invitrogen*, *Thermo Fisher Scientific*) and Alexa 546 goat

anti-rabbit (1:1000; A11035; *Invitrogen*, *Thermo Fisher Scientific*) were used as secondary antibodies.

Image acquisition. Confocal images of the LC were acquired in a Z-stack (2 µm step size) using an LSM 900 airyscan 2 microscope (*Zeiss*, Germany), controlled by the *ZEN* 3.1 imaging software, with laser intensities and gain of the photomultiplier tubes adjusted to maximize dynamic range while avoiding saturation of images. A Plan-APOCHROMAT 20X/0.8 objective was used, resulting in a field of view of 319.45 × 319.45 µm with a resolution of at least 1744 × 1744 pixels (183.2 nm/pixel). Some images were taken at a resolution of 2044 × 2044 pixels (i.e., 0.156 nm/pixel), and subsequently down-sampled to match the resolution of 1744 × 1744 pixels. Whole slices were imaged using a *Zeiss AxioObserver* epifluorescence microscope (*Zeiss*, Germany) with a Plan-APOCHROMAT 20X/0.8 objective, controlled by the *ZEN* 3.3 imaging software imaging software. *ImageJ*[100] was used to adjust image brightness, contrast, and create maximum intensity Z-projections.

Image analysis. Transgene expression was detected at the cellular level using the deep-learning-based algorithm *CellPose*[32]. In a first run, we analyzed all images from all approaches semi-automatically (i.e., automatically segmented cells were manually curated). We then used the obtained cell masks to re-train *CellPose*[33] in order to adapt it to our dataset (Supplementary material 2). In the second run, we used the re-trained model for automatic cell segmentation without any manual annotation. Segmentation was done separately for each channel, resulting in a total of 2766/3638/2774/2699 TH^+ cells and 2293/4195/1861/3061 $eGFP^+$ cells in Dbh^{cre}, Net^{cre}, Th^{cre}, and PRS×8-animals respectively (33/39/31/30 brain slices; 11/12/11/10 transduced LC; n = 7/7/7/7 mice). The average number of TH^+ cells that were found per slice was 83.8 ± 19.3, 93.3 ± 15.7, 89.5 ± 16.0, and 90.0 ± 15.3 cells (mean ± standard deviation) for Dbh^{cre}, Net^{cre}, Th^{cre}, and PRS×8, respectively. Cell detection was cross-validated with quantification by two different experimenters, who counted stained cells with the cell counter function of *ImageJ*. Cell masks of segmented cells in the *eGFP* and *TH* channels exported from *CellPose* where then checked for overlap using custom-written *MATLAB* scripts (*The MathWorks*). For quantification of transduction efficacy, co-expression was checked based on the cell masks in the *TH* channel, and masks which had an overlap of ≥ 50% with the masks in the *GFP* channel were defined as co-expressing. Similarly, co-expression was quantified based on the cell masks in the *GFP* channel, in order to quantify the specificity of transduction. The number of TH^+, GFP^+, and *TH-GFP*-co-expressing cells was subsequently summed up per animal, in order to avoid biasing the results based on (i) the different amount of TH^+ cells on individual slices and (ii) the total amount of slices taken from each animal (some slices had to be excluded due to tissue damage during the mounting process). Quantification of the effect of anti-*GFP* immunostaining on cell fluorescence was performed by fitting (least-squares) a binormal model of the form $f_R = \phi(\text{bias} + \text{gain} \times \phi^{-1}(f_G)) + \varepsilon$ with $\varepsilon \sim N(0,\sigma^2)$; and where f_R and f_G denotes the fluorescence in the red (*GFP*-stained) and green (native *eGFP*) channels respectively, and ϕ corresponds to the normal cumulative distribution function. Comparisons between the two channels have been

performed based on the cell masks detected in the *GFP*-stained channel, as we aimed to reveal additional cells upon *GFP* staining, which, by definition, are not detected in the native *eGFP* channel.

Behavioral screening. All behavioral experiments were performed in a quiet, darkened room by the same (female) experimenter, blind to the animal's genotype. Animals (genotype-, age- and sex-matched littermates, max. 2 animals of the same genotype and sex per litter) between 12 and 15 weeks of age at the start of the experiment were handled for 5 minutes (manually picked up and let to freely explore the experimenter's hands and arms) every other day in order to habituate mice to the experimenter. All experiments were video-recorded with a regular (when experiments were performed under illumination) or an infrared camera (when experiments were performed in darkness). All reported measures were performed using the software *Ethovision* XT17 (*Noldus*, Netherlands), unless stated otherwise. *Open Field Test.* An open field arena of 50 × 50 × 40 cm, homogeneously illuminated with white light of 25 lux, was used. At the start of the experiment, mice were placed in one corner of the box, and their movement was tracked for the following 20 minutes. The time spent in the center (the central 20 × 20 cm) and borders (5 cm from the walls) of the arena, the number of center crossings, and the latency to enter the arena center for the first time served as proxies for anxiety-like behavior, while the total travel distance served as a proxy for spontaneous locomotion. *Elevated Plus Maze*. The elevated plus maze consisted of four arms (30 × 5 cm) radiating from a central platform (5 × 5 cm), elevated 75 cm from the ground. Two opposing arms are covered by opaque walls (height: 17 cm), while the two other arms remain open. Mice were placed on the central platform and left to explore the maze for 5 minutes in total darkness. The time spent on opened versus closed arms, the number of entries to open arms, the fraction of open arm entries upon which mice went to the distant edge of the exposed arm, and the latency to leave the center of the maze served as proxies for anxiety-like behavior. In addition, the number of rearing events, the latency to the first rearing event, and the percentage of time spent grooming served as indirect measure for the absence of anxiety. EPM data acquisition and analysis were performed using *Observer* XT11 (*Noldus*, Netherlands). *Y-maze*. The maze consisted of three symmetrically radiating arms (34 × 5 cm), surrounded by walls (height: 30 cm) made of transparent plastic, with spatial cues placed behind each wall, homogeneously illuminated with white light of 10 lux. Mice were placed in the center of the maze and left to explore the maze until 26 transitions (entry to one arm with all four paws) between neighboring arms were made, or for a maximum of 15 minutes. Entering an arm after having visited the two other arms before, that is entering all three arms of the maze in one sequence, was considered a complete alternation. The fraction of alternations over all transitions (a proxy for working memory) as well as the time per transition (a proxy for exploratory behavior) was manually extracted. *Morris Water Maze*. The water maze consisted of a circular pool (diameter: 145 cm) filled with opaque water (19-21°C) with non-toxic white paint, surrounded by black curtains, and homogeneously illuminated with white light of 60 lux. A platform (diameter: 14 cm) was placed 1 cm below the water surface

in one of the four quadrants of the maze. Four landmarks (35 × 35 cm) of different shapes and grey tones were placed on the walls of the maze to allow for orientation. Animals were familiarized with swimming, platform searching, and handling in a pre-training session using a small, rectangular water-tank. Mice had to search for a platform in three trials (10-20 minutes inter-trial intervals), with a different platform location each time. Animals were transferred back to their home cage, where heat lamps were provided. On training day 1 and 2, animals underwent 4 training trials each (max. 90s), with varying starting positions. Once they climbed the platform, they were left to wait there for 10 s before being transferred back to the home cage. Animals that did not find the platform within 90 s were guided to the platform until they climbed it and left to wait on the platform for 10 s, before being transferred back to the home cage. On day 2, after the second training trial, and on day 3, a probe trial (60 s duration) without the platform was conducted. The time spent in the area where the platform was previously located, the time spent in the quadrant that previously contained the platform, the latency to the platform area, and the average minimum distance to the platform area were used to approximate successful spatial learning and memory. The total travel distance served as a measure for locomotor behavior, and the average distance to the wall were analyzed to compare thigmotactic behavior as well as searching strategies (i.e., circling around the pool).

Fiber photometry recordings. Approximately 3 weeks after surgery, animals were habituated to the experimenter, set-up, and head fixation on a linear treadmill (200–100 500 2100 and 700–100 100 0010; *Luigs & Neumann*), which for these experiments was immobilized, so animals would stay passive. Fiber photometry recordings were performed with the *pyPhotometry* system[101] (*Open Ephys*) controlling a multicolor LED light source (pE-4000; *CoolLED*) connected to the input ports of a dichroic cube (FMC5_E1(400–480)_F1(500–540)_E2(555-570)_F2(580–680)_S; *Doric Lenses*) as reported previously[11]. In brief, excitation light for quasi-isosbestic (405/10 nm) and calcium-dependent (470/10 nm) activation of jGCaMP8m was delivered in a temporally interleaved manner into the 400-480 nm input port of the dichroic cube, while excitation light for jRGECO1a (555-570 nm) was delivered via the 555-570 nm port. We also included excitation at 405/10 nm as a control channel when using jRGECO1a, as the indicator has been shown to be largely insensitive to calcium when excited at this wavelength[102], but we note that the efficiency of jRGECO1a excitation at 405 nm is very low (which, to a milder degree, is also true for jGCaMP8m). Hence, the recorded signal, which besides indicator fluorescence also contains autofluorescence originating from fiber optics and brain tissue[103], is likely composed differently and should not be over-interpreted. Emission light between 500-540 nm (jGCaMP8m) and 580-680 nm (jRGECO1a) was measured using a photodetector (DFD_FOA_FC; *Doric Lenses*), and digitized by the *pyPhotometry*-board at 130 Hz. Mice were connected to the dichroic cube with a low-autofluorescence patch cord (MFP_400/430/3000-0.57_1m_FC-ZF1.25(F)_LAF: 400 µm diameter, 0.57 NA; *Doric lenses*) via a zirconia mating sleeve (SLEEVE_ZR_1.25; *Doric Lenses*). Simultaneously, the left eye of the mouse was monitored using a monochrome camera equipped with a macro-objective (DMK 22UX249 and TMN 1.0/50; *The Imaging Source*) and a 780 nm long-pass filter (FGL780;

Thorlabs) under infrared illumination. Single video frames were triggered at 30 Hz with a voltage signal provided by an NI-DAQ-card (PCIe-6323; *National Instruments*), which was in addition fed to the *pyPhotometry* system for data synchronization.

Fiber photometry analysis. Raw traces of quasi-isosbestic and ligand-dependent fluorescence were detrended by fitting an exponential function to the respective trace and dividing the trace by the fitted curve, before being band-pass filtered (1/30-20 Hz; 4th order Butterworth filter) using *MATLAB*'s 'butter', and 'filtfilt' functions in order to remove signal components resulting from indicator bleaching and high frequency noise. The difference between the corrected functional and quasi-isosbestic traces was then taken as the functional signal, ΔF. Pupil edges (horizontal, vertical, and both diagonals) were extracted from each frame using *DeepLabCut*[62], and the pupil diameter was defined as the average distance of opposing edges in each frame. The pupil diameter was then resampled to match the sampling frequency of photometry recordings (130 Hz), and smoothed with a window size of 250 ms (using the *MATLAB* functions 'resample' and 'smooth'). Calcium transients in the photometry signal were detected using *MATLAB*'s 'findpeaks' function, with a minimum peak prominence of the mean plus three standard deviation of the whole trace, and a minimum peak distance of 10 seconds. Fiber photometry and pupil diameter recordings were then then cropped and aligned in a time window starting 2 seconds before and ending 10 seconds after each peak.

Statistics. For histological data, one-way ANOVA was performed; when significant, post-hoc comparisons between groups were performed using Tukey's honestly significant difference criterion which controls for inflated risk of type-1 error (false positives) following multiple comparisons (using *MATLAB*'s 'anova1' and 'multcompare' functions). For behavioral data, two-way ANOVA was performed to identify differences between genotypes, sexes, and interactions thereof, using the software *Graphpad Prism*. All statistical tests were two-tailed, with a type-1 error risk set to $\alpha = 0.05$. In all figures, error bars correspond to standard error of the mean.

Author contributions:

CW: Investigation, Validation, Data curation, Formal analysis, Writing – review & editing. **LSE**: Investigation, Validation, Data curation, Formal analysis, Visualization, Writing – review & editing. **MM**: Validation, Data curation, Formal analysis, Visualization, Software, Writing – review & editing, Funding acquisition. **KS**: Investigation, Validation, Writing – review & editing. **FM**: Validation, Methodology, Writing – review & editing, Supervision, Resources. **JSW**: Conceptualization, Methodology, Validation, Writing – review & editing, Supervision, Resources, Funding acquisition. **AD**: Conceptualization, Investigation, Validation, Data curation, Formal analysis, Visualization, Software, Writing – original draft, Writing – review & editing, Supervision

Acknowledgements: The authors gratefully acknowledge Dr. Ingke Braren for production of viral constructs and Stefan Schillemeit for expert technical support with histology. We thank Prof. Dr. Bernardo Sabatini for the kindly gifting the rAAV2/9-EF1a-DO-DIO-tdTomato-eGFP construct (*AddGene* plasmid #37120), the GENIE Project for gifting pGP-AAV-syn-jGCaMP8m-WPRE (*AddGene* plasmid #162375), Douglas Kim, *PhD*, and the GENIE Project for gifting pGP-CMV-NES-jRGECO1a (*AddGene* plasmid #61563), and Prof. Dr. Susumu Tonegawa for kindly providing the *Net*^{cre} line. We thank Patricia Jensen, *PhD*, and Nick Plummer, *PhD*, for helpful discussions on the different approaches of creating transgenic mouse lines. MM is supported by the *Alexander von Humboldt Stiftung*, and by the *Fondation Bettencourt-Schueller*. This work was supported by the German Research Foundation (DFG, grant agreement: 178316478-B8 to JSW).

Conflict of interest: The authors declare no conflict of interest.

References

1. Sturrock, R. R. & Rao, K. A. A QUANTITATIVE HISTOLOGICAL STUDY OF NEURONAL LOSS FROM THE LOCUS COERULEUS OF AGEING MICE. *Neuropathol. Appl. Neurobiol.* **11**, 55–60 (1985).
2. Poe, G. R. *et al.* Locus coeruleus: a new look at the blue spot. *Nat. Rev. Neurosci.* **21**, 644–659 (2020).
3. Chandler, D. J. *et al.* Redefining Noradrenergic Neuromodulation of Behavior: Impacts of a Modular Locus Coeruleus Architecture. *J. Neurosci. Off. J. Soc. Neurosci.* **39**, 8239–8249 (2019).
4. Schwarz, L. A. & Luo, L. Organization of the locus coeruleus-norepinephrine system. *Curr. Biol. CB* **25**, R1051–R1056 (2015).
5. Szot, P. Common factors among Alzheimer's disease, Parkinson's disease, and epilepsy: possible role of the noradrenergic nervous system. *Epilepsia* **53 Suppl 1**, 61–66 (2012).
6. Morris, L. S., McCall, J. G., Charney, D. S. & Murrough, J. W. The role of the locus coeruleus in the generation of pathological anxiety. *Brain Neurosci. Adv.* **4**, 2398212820930321 (2020).
7. McBurney-Lin, J., Lu, J., Zuo, Y. & Yang, H. Locus coeruleus-norepinephrine modulation of sensory processing and perception: A focused review. *Neurosci. Biobehav. Rev.* **105**, 190–199 (2019).

8. Aston-Jones, G. & Waterhouse, B. Locus coeruleus: From global projection system to adaptive regulation of behavior. *Brain Res.* **1645**, 75–78 (2016).
9. Waterhouse, B. D. & Navarra, R. L. The locus coeruleus-norepinephrine system and sensory signal processing: A historical review and current perspectives. *Brain Res.* **1709**, 1–15 (2019).
10. Tanguay, E., Bouchard, S.-J., Lévesque, M., De Koninck, P. & Breton-Provencher, V. Shining light on the noradrenergic system. *Neurophotonics* **10**, (2023).
11. Kagiampaki, Z. *et al.* Sensitive multicolor indicators for monitoring norepinephrine in vivo. *Nat. Methods* (2023) doi:10.1038/s41592-023-01959-z.
12. Feng, J. *et al.* A Genetically Encoded Fluorescent Sensor for Rapid and Specific In Vivo Detection of Norepinephrine. *Neuron* **102**, 745-761.e8 (2019).
13. Sun, F. *et al.* A Genetically Encoded Fluorescent Sensor Enables Rapid and Specific Detection of Dopamine in Flies, Fish, and Mice. *Cell* **174**, 481-496.e19 (2018).
14. Patriarchi, T. *et al.* Ultrafast neuronal imaging of dopamine dynamics with designed genetically encoded sensors. *Science* **360**, eaat4422 (2018).
15. Patriarchi, T. *et al.* An expanded palette of dopamine sensors for multiplex imaging in vivo. *Nat. Methods* **17**, 1147–1155 (2020).
16. Gong, S. *et al.* Targeting Cre Recombinase to Specific Neuron Populations with Bacterial Artificial Chromosome Constructs. *J. Neurosci.* **27**, 9817–9823 (2007).
17. Tillage, R. P. *et al.* Elimination of galanin synthesis in noradrenergic neurons reduces galanin in select brain areas and promotes active coping behaviors. *Brain Struct. Funct.* **225**, 785–803 (2020).
18. Yu, J. *et al.* Cell-specific expression of Cre recombinase in rat noradrenergic neurons via CRISPR-Cas9 system. *Neuroscience* S0306452224003452 (2024) doi:10.1016/j.neuroscience.2024.07.032.
19. Wagatsuma, A. *et al.* Locus coeruleus input to hippocampal CA3 drives single-trial learning of a novel context. *Proc. Natl. Acad. Sci.* **115**, E310–E316 (2018).

20. Savitt, J. M., Jang, S. S., Mu, W., Dawson, V. L. & Dawson, T. M. Bcl-x is required for proper development of the mouse substantia nigra. *J. Neurosci. Off. J. Soc. Neurosci.* **25**, 6721–6728 (2005).

21. Lindeberg, J. *et al.* Transgenic expression of Cre recombinase from the tyrosine hydroxylase locus: Transgenic Expression of Cre Recombinase. *genesis* **40**, 67–73 (2004).

22. Witten, I. B. *et al.* Recombinase-Driver Rat Lines: Tools, Techniques, and Optogenetic Application to Dopamine-Mediated Reinforcement. *Neuron* **72**, 721–733 (2011).

23. Hwang, D. Y., Carlezon, W. A., Isacson, O. & Kim, K. S. A high-efficiency synthetic promoter that drives transgene expression selectively in noradrenergic neurons. *Hum. Gene Ther.* **12**, 1731–1740 (2001).

24. Bacon, T. J., Pickering, A. E. & Mellor, J. R. Noradrenaline Release from Locus Coeruleus Terminals in the Hippocampus Enhances Excitation-Spike Coupling in CA1 Pyramidal Neurons Via β-Adrenoceptors. *Cereb. Cortex* **30**, 6135–6151 (2020).

25. Li, Y. *et al.* Retrograde optogenetic characterization of the pontospinal module of the locus coeruleus with a canine adenoviral vector. *Brain Res.* **1641**, 274–290 (2016).

26. Hayat, H. *et al.* Locus coeruleus norepinephrine activity mediates sensory-evoked awakenings from sleep. *Sci. Adv.* **6**, eaaz4232 (2020).

27. Schmidt-Supprian, M. & Rajewsky, K. Vagaries of conditional gene targeting. *Nat. Immunol.* **8**, 665–668 (2007).

28. Harno, E., Cottrell, E. C. & White, A. Metabolic pitfalls of CNS Cre-based technology. *Cell Metab.* **18**, 21–28 (2013).

29. Matthaei, K. I. Genetically manipulated mice: a powerful tool with unsuspected caveats. *J. Physiol.* **582**, 481–488 (2007).

30. Sohal, V. S., Zhang, F., Yizhar, O. & Deisseroth, K. Parvalbumin neurons and gamma rhythms enhance cortical circuit performance. *Nature* **459**, 698–702 (2009).

31. Hitoshi, N., Ken-ichi, Y. & Jun-ichi, M. Efficient selection for high-expression transfectants with a novel eukaryotic vector. *Gene* **108**, 193–199 (1991).

32. Stringer, C., Wang, T., Michaelos, M. & Pachitariu, M. Cellpose: a generalist algorithm for cellular segmentation. *Nat. Methods* **18**, 100–106 (2021).

33. Pachitariu, M. & Stringer, C. Cellpose 2.0: how to train your own model. *Nat. Methods* **19**, 1634–1641 (2022).

34. George Paxinos & Keith B.J. Franklin. *Paxinos and Franklin's the Mouse Brain in Stereotaxic Coordinates, Compact: The Coronal Plates and Diagrams*. (2019).

35. Fischer, K. B., Collins, H. K. & Callaway, E. M. Sources of off-target expression from recombinase-dependent AAV vectors and mitigation with cross-over insensitive ATG-out vectors. *Proc. Natl. Acad. Sci. U. S. A.* 201915974 (2019) doi:10.1073/pnas.1915974116.

36. Saunders, A., Johnson, C. A. & Sabatini, B. L. Novel recombinant adeno-associated viruses for Cre activated and inactivated transgene expression in neurons. *Front. Neural Circuits* **6**, (2012).

37. Rorabaugh, J. M. *et al.* Chemogenetic locus coeruleus activation restores reversal learning in a rat model of Alzheimer's disease. *Brain* **140**, 3023–3038 (2017).

38. Stevens, L. *et al.* Optimized Parameters for Transducing the Locus Coeruleus Using Canine Adenovirus Type 2 (CAV2) Vector in Rats for Chemogenetic Modulation Research. *Front. Neurosci.* **15**, 663337 (2021).

39. Chen, E. *et al.* Altered Baseline and Nicotine-Mediated Behavioral and Cholinergic Profiles in ChAT-Cre Mouse Lines. *J. Neurosci. Off. J. Soc. Neurosci.* **38**, 2177–2188 (2018).

40. Costa, K. M., Schenkel, D. & Roeper, J. Sex-dependent alterations in behavior, drug responses and dopamine transporter expression in heterozygous DAT-Cre mice. *Sci. Rep.* **11**, 3334 (2021).

41. Chohan, M. O., Esses, S., Haft, J., Ahmari, S. E. & Veenstra-VanderWeele, J. Altered baseline and amphetamine-mediated behavioral profiles in dopamine transporter Cre (DAT-Ires-Cre) mice compared to tyrosine hydroxylase Cre (TH-Cre) mice. *Psychopharmacology (Berl.)* **237**, 3553–3568 (2020).

42. Morris, L. S., McCall, J. G., Charney, D. S. & Murrough, J. W. The role of the locus coeruleus in the generation of pathological anxiety. *Brain Neurosci. Adv.* **4**, 239821282093032 (2020).

43. Ross, J. A. & Van Bockstaele, E. J. The Locus Coeruleus- Norepinephrine System in Stress and Arousal: Unraveling Historical, Current, and Future Perspectives. *Front. Psychiatry* **11**, 601519 (2021).

44. Belzung, C. Chapter 4.11 Measuring rodent exploratory behavior. in *Techniques in the Behavioral and Neural Sciences* vol. 13 738–749 (Elsevier, 1999).

45. Pellow, S., Chopin, P., File, S. E. & Briley, M. Validation of open : closed arm entries in an elevated plus-maze as a measure of anxiety in the rat. *J. Neurosci. Methods* **14**, 149–167 (1985).

46. Kempadoo, K. A., Mosharov, E. V., Choi, S. J., Sulzer, D. & Kandel, E. R. Dopamine release from the locus coeruleus to the dorsal hippocampus promotes spatial learning and memory. *Proc. Natl. Acad. Sci.* **113**, 14835–14840 (2016).

47. Takeuchi, T. *et al.* Locus coeruleus and dopaminergic consolidation of everyday memory. *Nature* **537**, 357–362 (2016).

48. Lalonde, R. The neurobiological basis of spontaneous alternation. *Neurosci. Biobehav. Rev.* **26**, 91–104 (2002).

49. Steinberg, H., Rushton, R. & Tinson, C. Modification of the Effects of an Amphetamine–Barbiturate Mixture by the Past Experience of Rats. *Nature* **192**, 533–535 (1961).

50. Morris, R. G. M. Spatial localization does not require the presence of local cues. *Learn. Motiv.* **12**, 239–260 (1981).

51. Kabanova, A., Cavani, E., Logothetis, N. K. & Eschenko, O. Feasibility of Canine Adenovirus Type 2 (CAV2) Based Vector for the Locus Coeruleus Optogenetic Activation in Non-Transgenic Rats: Implications for Functional Studies. *Brain Sci.* **12**, 904 (2022).

52. Vazey, E. M. & Aston-Jones, G. Designer receptor manipulations reveal a role of the locus coeruleus noradrenergic system in isoflurane general anesthesia. *Proc. Natl. Acad. Sci.* **111**, 3859–3864 (2014).

53. Zhang, Y. *et al.* Fast and sensitive GCaMP calcium indicators for imaging neural populations. *Nature* (2023) doi:10.1038/s41586-023-05828-9.

54. Dana, H. *et al.* Sensitive red protein calcium indicators for imaging neural activity. *eLife* **5**, e12727 (2016).

55. Breton-Provencher, V. & Sur, M. Active control of arousal by a locus coeruleus GABAergic circuit. *Nat. Neurosci.* **22**, 218–228 (2019).

56. Klapoetke, N. C. *et al.* Independent optical excitation of distinct neural populations. *Nat. Methods* **11**, 338–346 (2014).

57. Shaner, N. C. *et al.* Improved monomeric red, orange and yellow fluorescent proteins derived from Discosoma sp. red fluorescent protein. *Nat. Biotechnol.* **22**, 1567–1572 (2004).

58. Mahn, M. *et al.* High-efficiency optogenetic silencing with soma-targeted anion-conducting channelrhodopsins. *Nat. Commun.* **9**, 4125 (2018).

59. Cormack, B. P., Valdivia, R. H. & Falkow, S. FACS-optimized mutants of the green fluorescent protein (GFP). *Gene* **173**, 33–38 (1996).

60. Hofherr, A., Fakler, B. & Klöcker, N. Selective Golgi export of Kir2.1 controls the stoichiometry of functional Kir2.x channel heteromers. *J. Cell Sci.* **118**, 1935–1943 (2005).

61. Lim, S. T., Antonucci, D. E., Scannevin, R. H. & Trimmer, J. S. A Novel Targeting Signal for Proximal Clustering of the Kv2.1 K+ Channel in Hippocampal Neurons. *Neuron* **25**, 385–397 (2000).

62. Mathis, A. *et al.* DeepLabCut: markerless pose estimation of user-defined body parts with deep learning. *Nat. Neurosci.* **21**, 1281–1289 (2018).

63. Vincent, S. R. Distributions of tyrosine hydroxylase-, dopamine-beta-hydroxylase-, and phenylethanolamine-N-methyltransferase-immunoreactive neurons in the brain of the hamster (Mesocricetus auratus). *J. Comp. Neurol.* **268**, 584–599 (1988).

64. Qin, H., Lu, J., Jin, W., Chen, X. & Fu, L. Multichannel fiber photometry for mapping axonal terminal activity in a restricted brain region in freely moving mice. *Neurophotonics* **6**, 1 (2019).

65. Pisanello, M. *et al.* The Three-Dimensional Signal Collection Field for Fiber Photometry in Brain Tissue. *Front. Neurosci.* **13**, 82 (2019).

66. Koga, K. *et al.* Ascending noradrenergic excitation from the locus coeruleus to the anterior cingulate cortex. *Mol. Brain* **13**, 49 (2020).

67. Nomura, S. *et al.* Combined Optogenetic Approaches Reveal Quantitative Dynamics of Endogenous Noradrenergic Transmission in the Brain. *iScience* **23**, 101710 (2020).

68. Nomura, S. *et al.* Noradrenalin and dopamine receptors both control cAMP-PKA signaling throughout the cerebral cortex. *Front. Cell. Neurosci.* **8**, 247 (2014).

69. Lavoie, A. & Liu, B. Canine Adenovirus 2: A Natural Choice for Brain Circuit Dissection. *Front. Mol. Neurosci.* **13**, 9 (2020).

70. Stevens, L. *et al.* A Feasibility Study to Investigate Chemogenetic Modulation of the Locus Coeruleus by Means of Single Unit Activity. *Front. Neurosci.* **14**, 162 (2020).

71. Antila, H. *et al.* A noradrenergic-hypothalamic neural substrate for stress-induced sleep disturbances. *Proc. Natl. Acad. Sci.* **119**, e2123528119 (2022).

72. Kempadoo, K. A., Mosharov, E. V., Choi, S. J., Sulzer, D. & Kandel, E. R. Dopamine release from the locus coeruleus to the dorsal hippocampus promotes spatial learning and memory. *Proc. Natl. Acad. Sci.* **113**, 14835–14840 (2016).

73. Lammel, S. *et al.* Diversity of transgenic mouse models for selective targeting of midbrain dopamine neurons. *Neuron* **85**, 429–438 (2015).

74. Min, N., Joh, T. H., Kim, K. S., Peng, C. & Son, J. H. 5' Upstream DNA sequence of the rat tyrosine hydroxylase gene directs high-level and tissue-specific expression to catecholaminergic neurons in the central nervous system of transgenic mice. *Mol. Brain Res.* **27**, 281–289 (1994).

75. Rukhadze, I. *et al.* Catecholaminergic A1/C1 neurons contribute to the maintenance of upper airway muscle tone but may not participate in NREM sleep-related depression of these muscles. *Respir. Physiol. Neurobiol.* **244**, 41–50 (2017).

76. Vuong, H. E., Pérez de Sevilla Müller, L., Hardi, C. N., McMahon, D. G. & Brecha, N. C. Heterogeneous transgene expression in the retinas of the TH-RFP, TH-Cre, TH-BAC-Cre and DAT-Cre mouse lines. *Neuroscience* **307**, 319–337 (2015).
77. Gábriel, R., Erdélyi, F., Szabó, G., Lawrence, J. J. & Wilhelm, M. Ectopic transgene expression in the retina of four transgenic mouse lines. *Brain Struct. Funct.* **221**, 3729–3741 (2016).
78. Cardozo Pinto, D. F. *et al.* Characterization of transgenic mouse models targeting neuromodulatory systems reveals organizational principles of the dorsal raphe. *Nat. Commun.* **10**, 4633 (2019).
79. Papathanou, M., Dumas, S., Pettersson, H., Olson, L. & Wallén-Mackenzie, Å. Off-Target Effects in Transgenic Mice: Characterization of Dopamine Transporter (DAT)-Cre Transgenic Mouse Lines Exposes Multiple Non-Dopaminergic Neuronal Clusters Available for Selective Targeting within Limbic Neurocircuitry. *eNeuro* **6**, (2019).
80. Hu, H., Cavendish, J. Z. & Agmon, A. Not all that glitters is gold: off-target recombination in the somatostatin-IRES-Cre mouse line labels a subset of fast-spiking interneurons. *Front. Neural Circuits* **7**, 195 (2013).
81. Zhang, B. *et al.* The specificity and role of microglia in epileptogenesis in mouse models of tuberous sclerosis complex. *Epilepsia* **59**, 1796–1806 (2018).
82. Stuber, G. D., Stamatakis, A. M. & Kantak, P. A. Considerations when using cre-driver rodent lines for studying ventral tegmental area circuitry. *Neuron* **85**, 439–445 (2015).
83. Song, A. J. & Palmiter, R. D. Detecting and Avoiding Problems When Using the Cre-lox System. *Trends Genet. TIG* **34**, 333–340 (2018).
84. Prabhakar, A., Vujovic, D., Cui, L., Olson, W. & Luo, W. Leaky expression of channelrhodopsin-2 (ChR2) in Ai32 mouse lines. *PLOS ONE* **14**, e0213326 (2019).
85. Mariscal, P. *et al.* Sexual differences in locus coeruleus neurons and related behavior in C57BL/6J mice. *Biol. Sex Differ.* **14**, 64 (2023).
86. An, X.-L. *et al.* Strain and Sex Differences in Anxiety-Like and Social Behaviors in C57BL/6J and BALB/cJ Mice. *Exp. Anim.* **60**, 111–123 (2011).

87. Fritz, A., Amrein, I. & Wolfer, D. P. Similar reliability and equivalent performance of female and male mice in the open field and water-maze place navigation task. *Am. J. Med. Genet. C Semin. Med. Genet.* **175**, 380–391 (2017).

88. Thanky, N. R., Son, J. H. & Herbison, A. E. Sex differences in the regulation of tyrosine hydroxylase gene transcription by estrogen in the locus coeruleus of TH9-LacZ transgenic mice. *Mol. Brain Res.* **104**, 220–226 (2002).

89. Sorge, R. E. *et al.* Olfactory exposure to males, including men, causes stress and related analgesia in rodents. *Nat. Methods* **11**, 629–632 (2014).

90. Georgiou, P. *et al.* Experimenters' sex modulates mouse behaviors and neural responses to ketamine via corticotropin releasing factor. *Nat. Neurosci.* **25**, 1191–1200 (2022).

91. Gouveia, K. & Hurst, J. L. Optimising reliability of mouse performance in behavioural testing: the major role of non-aversive handling. *Sci. Rep.* **7**, 44999 (2017).

92. Ueno, H. *et al.* Effects of repetitive gentle handling of male C57BL/6NCrl mice on comparative behavioural test results. *Sci. Rep.* **10**, 3509 (2020).

93. Mandillo, S. *et al.* Reliability, robustness, and reproducibility in mouse behavioral phenotyping: a cross-laboratory study. *Physiol. Genomics* **34**, 243–255 (2008).

94. Crabbe, J. C., Wahlsten, D. & Dudek, B. C. Genetics of Mouse Behavior: Interactions with Laboratory Environment. *Science* **284**, 1670–1672 (1999).

95. Uematsu, A. *et al.* Modular organization of the brainstem noradrenaline system coordinates opposing learning states. *Nat. Neurosci.* **20**, 1602–1611 (2017).

96. Botterill, J. J. *et al.* Off-Target Expression of Cre-Dependent Adeno-Associated Viruses in Wild-Type C57BL/6J Mice. *eneuro* **8**, ENEURO.0363-21.2021 (2021).

97. Haery, L. *et al.* Adeno-Associated Virus Technologies and Methods for Targeted Neuronal Manipulation. *Front. Neuroanat.* **13**, 93 (2019).

98. Baral, S. *et al.* Spike-Dependent Dynamic Partitioning of the Locus Coeruleus Network through Noradrenergic Volume Release in a Simulation of the Nucleus Core. *Brain Sci.* **12**, 728 (2022).

99. Matthies, H. J. *et al.* Subcellular localization of the antidepressant-sensitive norepinephrine transporter. *BMC Neurosci.* **10**, 65 (2009).

100. Schindelin, J. *et al.* Fiji: an open-source platform for biological-image analysis. *Nat. Methods* **9**, 676–682 (2012).

101. Akam, T. & Walton, M. E. pyPhotometry: Open source Python based hardware and software for fiber photometry data acquisition. *Sci. Rep.* **9**, 3521 (2019).

102. Molina, R. S. *et al.* Understanding the Fluorescence Change in Red Genetically Encoded Calcium Ion Indicators. *Biophys. J.* **116**, 1873–1886 (2019).

103. Formozov, A., Dieter, A. & Wiegert, J. S. A flexible and versatile system for multi-color fiber photometry and optogenetic manipulation. *Cell Rep. Methods* 100418 (2023) doi:10.1016/j.crmeth.2023.100418.

– Supplementary Material –

Supplementary table 1:	Cre driver lines to target the NE system in mice
Supplementary table 1:	Statistical analysis of behavioral screening
Supplementary Figure S1:	Independence of histology quantification on the overlap threshold of cell masks
Supplementary Figure S2:	Leakage of cre-dependent virus in wild-type mice
Supplementary Figure S3:	Agreement between *CellPose*-based and human-based cell segmentation
Supplementary Figure S4:	Comparison of native *eGFP* expression with anti-*GFP* staining
Supplementary Figure S5:	Ectopic transgene expression across model systems
Supplementary Figure S6:	Verification of LC transduction and viral spread
Supplementary Figure S7:	Supplementary readouts obtained in the open field test
Supplementary Figure S8:	Supplementary readouts obtained in the elevated plus maze
Supplementary Figure S9:	Supplementary readouts obtained in the Y-maze
Supplementary Figure S10:	Morris water maze during training sessions
Supplementary Figure S11:	Supplementary readouts obtained in the Morris water maze
Supplementary Figure S12:	Bleaching of calcium indicators in fiber photometry recordings from the LC

Supplementary table 1 | Cre driver lines to target the NE system in mice. Bold font indicates mouse lines used in this study. Grey font indicates mouse lines which are not readily available from any vendor.

strain name	*trivial name*	*gene*	*strategy*	*provider*	*strain ID*	*reference*
B6.Cg-Dbh$^{tm3.2(cre)Pjen}$/J	***Dbh^{cre}***	Dopamine-β-Hydroxylase	knock-in/ knock-out	*Jackson Laboratory*	033951	Tillage et al.[17]
Tg(Dbh-cre)KH210Gsat/Mmucd	*Dbh^{cre}*	Dopamine-β-Hydroxylase	BAC	*Mutant Mouse Resource & Research Centers*	036734-UCD	Gong et al.[16]
Tg(Dbh-cre)KH212Gsat/Mmucd	*Dbh^{cre}*	Dopamine-β-Hydroxylase	BAC	*Mutant Mouse Resource & Research Centers*	032081-UCD	Gong et al.[16]
B6.Cg-7630403G23 RikTg$^{(Th\text{-}cre)1Tmd}$/J	***Th^{cre}***	Tyrosine Hydroxylase	random insertion	*Jackson Laboratory*	008601	Savitt et al.[20]
B6.FVB(Cg)Tg(Th-cre)Fl172Gsat/Mmucd	*Th^{cre}*	Tyrosine Hydroxylase	BAC	*Mutant Mouse Resource & Research Centers*	031029-UCD	Gong et al.[16]
B6.129X1-Th$^{tm1(cre)Te}$/Kieg	*Th^{cre}*	Tyrosine Hydroxylase	Targeted mutation	*European Mouse Mutant Archive*	EM: 00254	Lindeberg et al.[21]
Tg(Slc6a2-cre)#Stl	***Net^{cre}***	Norepi-nephrine Transporter	BAC	–	–	Wagatsuma et al.[19]

Supplementary table 2 | Statistical analysis of behavioral screening. The table indicates results of a two-way ANOVA analyzing effects of genotype (GT), sex, or interactions thereof (×) in the mouse lines included in this study on different aspects of behavior in the in the open field test (OF), elevated plus maze (EPM), Y-maze (YM), and Morris water maze (MWM). All groups included 8 male and 8 female mice of each genotype. *p*-values below 0.05 are indicated in bold font. Note that multiple comparisons were not corrected in this table.

paradigm		***Dbh^{cre}***			***Net^{cre}***			***Th^{cre}***		
test	**readout**	**GT**	**Sex**	**×**	**GT**	**Sex**	**×**	**GT**	**Sex**	**×**
OF	*t* in center	$F = 0.45$ $p = 0.51$	$F = 0.39$ $p = 0.22$	$F = 1.60$ $p = 0.22$	$F = 0.54$ $p = 0.47$	$F = 3.93$ $p = 0.06$	$F = 0.01$ $p = 0.94$	$F = 0.01$ $p = 0.91$	$F = 4.22$ $p = 0.05$	$F = 4.37$ $p = 0.05$
	center crossings	$F = 0.01$ $p = 0.91$	$F = 0.41$ $p = 0.54$	$F = 1.87$ $p = 0.28$	$F = 0.02$ $p = 0.89$	$F = 0.14$ $p = 0.71$	$F = 0.05$ $p = 0.82$	$F = 0.01$ $p = 0.91$	$F = 1.34$ $p = 0.26$	$F = 0.33$ $p = 0.57$
	latency to center	$F = 1.33$ $p = 0.26$	$F = 1.00$ $p = 0.33$	$F = 0.11$ $p = 0.74$	$F = 1.27$ $p = 0.27$	$F = 0.29$ $p = 0.60$	$F = 1.00$ $p = 0.33$	$F = 1.10$ $p = 0.34$	$F = 2.96$ $p = 0.10$	$F = 2.89$ $p = 0.10$
	distance to wall	$F = 0.61$ $p = 0.44$	$F = 6.91$ **$p = 0.01$**	$F = 3.26$ $p = 0.08$	$F = 0.73$ $p = 0.4$	$F = 2.31$ $p = 0.54$	$F = 0.39$ $p = 0.14$	$F = 3.34$ $p = 0.08$	$F = 2.09$ $p = 0.16$	$F = 6.41$ **$p = 0.02$**
	t in border	$F = 1.52$ $p = 0.23$	$F = 11.7$ **$p < 0.01$**	$F = 1.44$ $p = 0.24$	$F = 2.81$ $p = 0.11$	$F = 1.82$ $p = 0.19$	$F = 0.07$ $p = 0.79$	$F = 1.74$ $p = 0.20$	$F = 0.37$ $p = 0.55$	$F = 3.72$ $p = 0.06$
	travel distance	$F = 0.03$ $p = 0.87$	$F = 0.28$ $p = 0.60$	$F = 0.03$ $p = 0.87$	$F = 0.54$ $p = 0.47$	$F = 3.93$ $p = 0.06$	$F < 0.01$ $p = 0.94$	$F = 0.01$ $p = 0.94$	$F = 16.4$ **$p < 0.01$**	$F < 0.01$ $p = 0.97$
	t in open arm	$F = 1.96$ $p = 0.17$	$F = 1.95$ $p = 0.17$	$F = 0.01$ $p = 0.91$	$F < 0.01$ $p = 0.93$	$F = 0.76$ $p = 0.39$	$F = 2.34$ $p = 0.14$	$F = 0.32$ $p = 0.57$	$F = 0.07$ $p = 0.79$	$F = 0.12$ $p = 0.73$

EPM	open arm entries	$F = 1.91$ $p = 0.22$	$F = 0.01$ $p = 0.91$	$F = 0.17$ $p = 0.68$	$F = 0.75$ $p = 0.60$	$F = 0.07$ $p = 0.80$	$F = 0.21$ $p = 0.65$	$F = 0.14$ $p = 0.71$	$F = 0.03$ $p = 0.87$	$F = 0.33$ $p = 0.57$
	open arm edges	$F < 0.01$ $p = 0.94$	$F = 5.52$ **$p = 0.03$**	$F = 0.30$ $p = 0.59$	$F < 0.01$ $p = 0.95$	$F = 3.57$ $p = 0.07$	$F = 0.16$ $p = 0.69$	$F < 0.01$ $p = 0.95$	$F = 3.57$ $p = 0.07$	$F = 0.16$ $p = 0.69$
	t to leave center	$F = 0.01$ $p = 0.91$	$F = 5.02$ $p = 0.03$	$F < 0.01$ $p = 0.98$	$F = 2.59$ $p = 0.12$	$F = 2.12$ $p = 0.16$	$F < 0.01$ $p = 0.94$	$F = 4.19$ $p = 0.05$	$F = 0.61$ $p = 0.44$	$F = 0.12$ $p = 0.73$
	Rearing events	$F = 2.13$ $p = 0.16$	$F = 1.45$ $p = 0.16$	$F = 2.13$ $p = 0.16$	$F = 0.81$ $p = 0.38$	$F = 3.20$ $p = 0.08$	$F < 0.01$ $p = 0.93$	$F = 0.91$ $p = 0.35$	$F = 2.43$ $p = 0.13$	$F = 0.12$ $p = 0.73$
	t to rearing	$F = 2.11$ $p = 0.16$	$F = 1.41$ $p = 0.24$	$F = 0.04$ $p = 0.85$	$F = 2.28$ $p = 0.15$	$F = 2.77$ $p = 0.11$	$F = 0.95$ $p = 0.34$	$F = 0.26$ $p = 0.61$	$F = 0.26$ $p = 0.61$	$F = 4.43$ **$p = 0.04$**
	t grooming	$F = 1.01$ $p = 0.32$	$F = 0.87$ $p = 0.36$	$F = 0.05$ $p = 0.82$	$F = 1.23$ $p = 0.26$	$F = 0.82$ $p = 0.37$	$F = 1.98$ $p = 0.17$	$F = 0.25$ $p = 0.62$	$F = 0.23$ $p = 0.63$	$F = 1.42$ $p = 0.24$
YM	alter-nations	$F = 1.30$ $p = 0.26$	$F = 1.62$ $p = 0.21$	$F = 0.24$ $p = 0.62$	$F = 2.48$ $p = 0.13$	$F = 2.32$ $p = 0.14$	$F = 0.02$ $p = 0.89$	$F = 0.23$ $p = 0.64$	$F = 2.95$ $p = 0.09$	$F = 0.31$ $p = 0.58$
	t/ transitions	$F = 0.04$ $p = 0.84$	$F = 0.76$ $p = 0.39$	$F = 2.55$ $p = 0.12$	$F = 3.04$ $p = 0.09$	$F = 2.95$ $p = 0.09$	$F = 0.31$ $p = 0.56$	$F = 3.04$ $p = 0.09$	$F = 0.20$ $p = 0.66$	$F = 11.2$ **$p < 0.01$**
MWM day 2	*t* in platform	$F = 0.40$ $p = 0.54$	$F = 0.16$ $p = 0.69$	$F = 0.66$ $p = 0.42$	$F = 0.70$ $p = 0.41$	$F = 0.07$ $p = 0.79$	$F = 1.3$ $p = 0.26$	$F = 0.03$ $p = 0.87$	$F = 0.93$ $p = 0.34$	$F < 0.01$ $p = 0.93$
	t in quadrant	$F = 0.48$ $p = 0.49$	$F < 0.01$ $p = 0.99$	$F = 0.07$ $p = 0.79$	$F = 0.23$ $p = 0.64$	$F = 3.01$ $p = 0.09$	$F = 0.31$ $p = 0.58$	$F < 0.01$ $p = 0.95$	$F = 0.32$ $p = 0.57$	$F < 0.01$ $p = 0.94$
	t to platform	$F = 0.90$ $p = 0.35$	$F = 0.06$ $p = 0.81$	$F = 0.08$ $p = 0.78$	$F = 0.03$ $p = 0.86$	$F = 0.32$ $p = 0.58$	$F = 0.60$ $p = 0.44$	$F =0.07$ $p = 0.79$	$F = 4.25$ $p = 0.05$	$F = 1.53$ $p = 0.23$
	distance to platform	$F = 0.23$ $p = 0.63$	$F = 1.63$ $p = 0.21$	$F = 2.40$ $p = 0.13$	$F = 0.26$ $p = 0.62$	$F = 2.96$ $p = 0.10$	$F < 0.01$ $p = 0.95$	$F = 0.05$ $p = 0.82$	$F = 1.30$ $p = 0.26$	$F = 0.27$ $p = 0.61$
	travel distance	$F = 0.04$ $p = 0.53$	$F = 0.29$ $p = 0.60$	$F = 0.58$ $p = 0.45$	$F = 0.88$ $p = 0.36$	$F = 2.48$ $p = 0.13$	$F = 0.02$ $p = 0.88$	$F = 0.04$ $p = 0.84$	$F < 0.01$ $p = 0.99$	$F = 0.46$ $p = 0.51$
	distance to wall	$F = 1.57$ $p = 0.24$	$F = 1.47$ $p = 0.24$	$F = 1.00$ $p = 0.32$	$F = 0.03$ $p = 0.87$	$F < 0.01$ $p = 0.99$	$F = 0.92$ $p = 0.35$	$F = 0.86$ $p = 0.36$	$F = 1.42$ $p = 0.24$	$F = 0.23$ $p = 0.63$
MWM day 3	*t* in platform	$F = 1.14$ $p = 0.29$	$F = 0.80$ $p = 0.38$	$F < 0.01$ $p = 0.94$	$F = 0.56$ $p = 0.46$	$F = 0.43$ $p = 0.52$	$F = 0.30$ $p = 0.59$	$F = 0.34$ $p = 0.56$	$F = 0.30$ $p = 0.59$	$F = 0.33$ $p = 0.57$
	t in quadrant	$F = 0.04$ $p = 0.85$	$F = 1.50$ $p = 0.23$	$F = 0.41$ $p = 0.52$	$F = 0.68$ $p = 0.42$	$F = 0.45$ $p = 0.51$	$F = 0.25$ $p = 0.62$	$F = 0.59$ $p = 0.45$	$F = 0.25$ $p = 0.62$	$F = 0.16$ $p = 0.69$
	t to platform	$F = 0.07$ $p = 0.80$	$F = 0.29$ $p = 0.60$	$F = 0.11$ $p = 0.75$	$F = 0.14$ $p = 0.71$	$F = 1.59$ $p = 0.22$	$F = 0.40$ $p = 0.53$	$F < 0.01$ $p = 0.97$	$F = 0.24$ $p = 0.63$	$F = 0.40$ $p = 0.53$
	distance to platform	$F = 0.11$ $p = 0.75$	$F = 0.49$ $p = 0.49$	$F = 0.01$ $p = 0.91$	$F = 0.88$ $p = 0.36$	$F = 0.09$ $p = 0.76$	$F = 2.84$ $p = 0.10$	$F = 0.07$ $p = 0.80$	$F = 4.0$ $p = 0.06$	$F = 0.04$ $p = 0.83$
	travel distance	$F = 0.06$ $p = 0.82$	$F = 0.28$ $p = 0.60$	$F = 0.55$ $p = 0.47$	$F = 1.24$ $p = 0.27$	$F = 0.79$ $p = 0.38$	$F = 0.05$ $p = 0.82$	$F = 0.13$ $p = 0.73$	$F = 0.05$ $p = 0.82$	$F < 0.01$ $p = 0.93$
	distance to wall	$F = 2.94$ $p = 0.10$	$F = 0.17$ $p = 0.69$	$F = 0.89$ $p = 0.35$	$F = 0.07$ $p = 0.79$	$F = 2.28$ $p = 0.14$	$F = 0.11$ $p = 0.75$	$F < 0.01$ $p = 0.93$	$F = 2.87$ $p = 0.10$	$F = 0.48$ $p = 0.50$

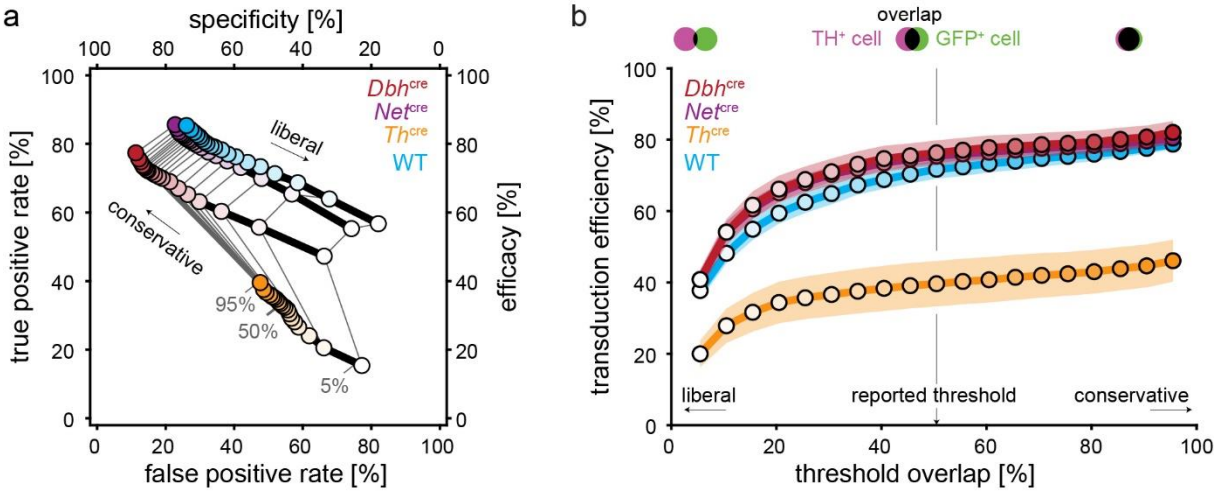

Figure S1 | Independence of histology quantification on the overlap threshold of cell masks. a, Efficacy and specificity from the 4 different model systems (as in Figure 1d) as a function of the threshold overlap parameter (light to dark colors; ranging from 5% to 95%, in steps of 5%) which defines the minimal overlap between *GFP*⁺ and *TH*⁺ channels for a *TH*⁺ cell to be also labeled as *GFP*⁺. **b**, Transduction efficiency (summarizing sensitivity and specificity in a single metric) from the 4 different model systems (as in Figure 1e) quantitatively varied as a function of the threshold overlap parameter. Importantly, conclusions were robust to this parameter choice as shown by the non-crossing of the curves. In the main text, we report values for a neutral threshold overlap parameter of 50%. Shading areas denote the standard error of the mean (n = 7).

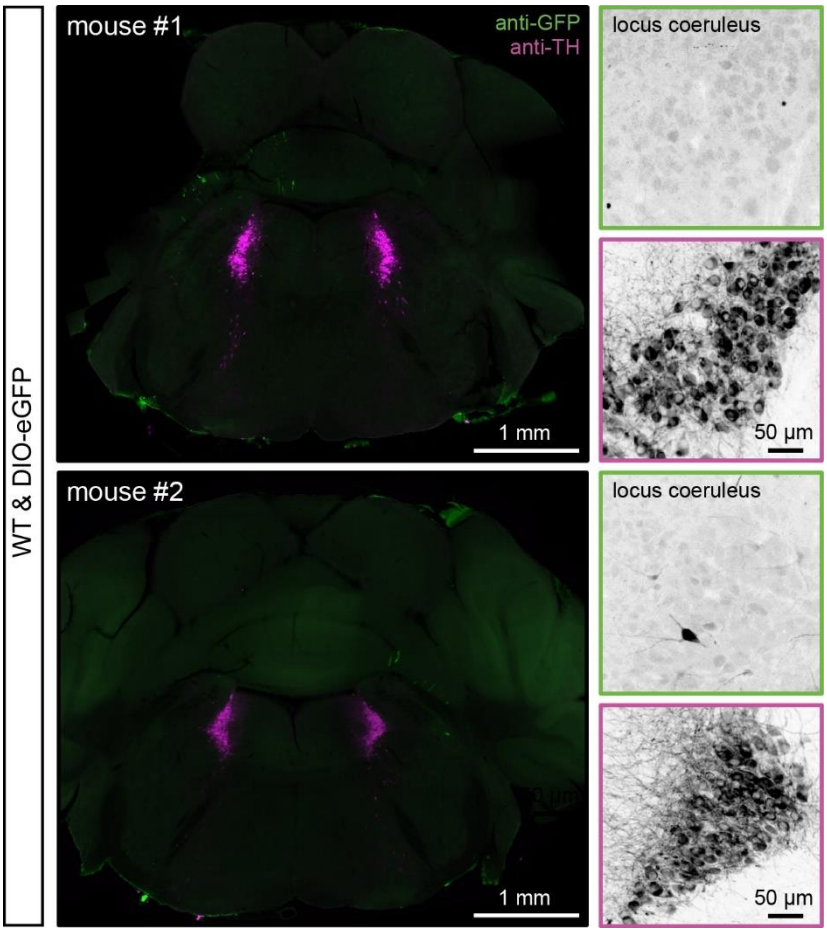

Figure S2 | Leakage of cre-dependent virus in wild-type mice. Immunohistochemical staining against *GFP* (green) and *TH* (magenta) in two wild-type mice injected with rAAV2/9-DIO-eGFP. *eGFP* expression was only observed in very few cells both within and outside of the LC.

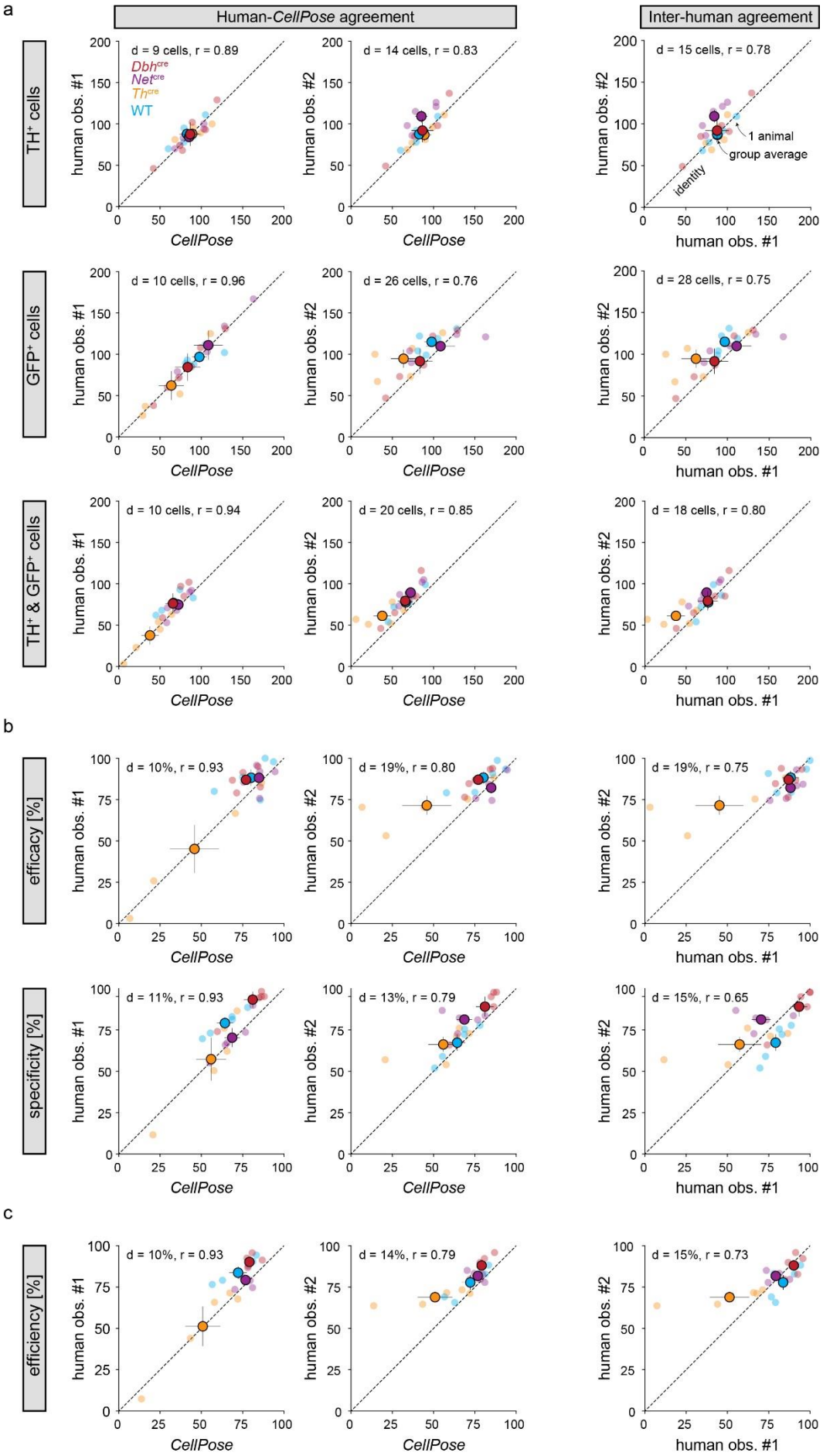
a
Human-CellPose agreement
Inter-human agreement
TH+ cells
GFP+ cells
TH+ & GFP+ cells
d = 9 cells, r = 0.89
Dbhcre
Netcre
Thcre
WT
d = 14 cells, r = 0.83
d = 15 cells, r = 0.78
1 animal
group average
identity
d = 10 cells, r = 0.96
d = 26 cells, r = 0.76
d = 28 cells, r = 0.75
d = 10 cells, r = 0.94
d = 20 cells, r = 0.85
d = 18 cells, r = 0.80
human obs. #1
human obs. #2
CellPose
b
efficacy [%]
specificity [%]
d = 10%, r = 0.93
d = 19%, r = 0.80
d = 19%, r = 0.75
d = 11%, r = 0.93
d = 13%, r = 0.79
d = 15%, r = 0.65
c
efficiency [%]
d = 10%, r = 0.93
d = 14%, r = 0.79
d = 15%, r = 0.73

Figure S3 | Agreement between *CellPose*-based and human-based cell segmentation. a, Correlation of cell counts; **b**, Efficacy & specificity; **c**, transduction efficiency between cells identified by *CellPose* vs. labeled by each of the two human observers (AD and CW; first 2 columns); and between the two human observers (3rd column). A total of 5 slices of 5 different mice were used for each of the 4 model systems. Dashed lines indicate identity. In each case, two measures of agreement are reported: Pearson's correlation coefficient, denoted as r; and the distance between observers, denoted as $d = \sqrt{\sum_i (x_i - y_i)^2}$ where x and y correspond to observers' reports (**a**) or derived quantities (**b**, **c**), and i to the brain slice. Error bars denote the standard error of the mean (with $n = 5$).

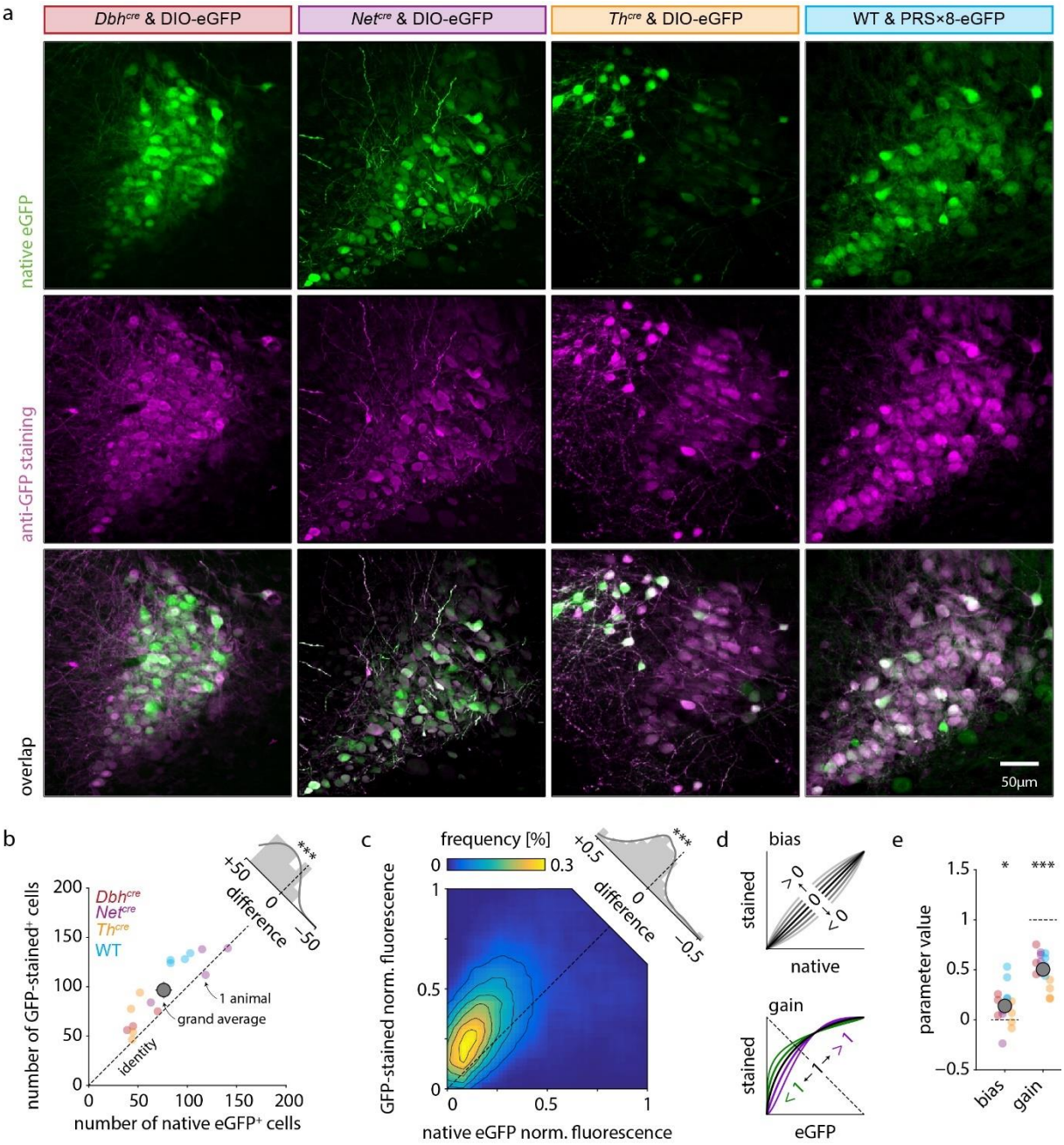

Figure S4 | Comparison of native *eGFP* expression with anti-*GFP* staining. a, Example images of brain slices showing native *eGFP* fluorescence (green, top) and anti-*GFP* immunofluorescence with a secondary antibody in the red spectrum (magenta, center) in *Dbh*^{cre}, *Net*^{cre}, *Th*^{cre} and PRS×8 mice (from left to right). **b**, Number of neurons detected by *CellPose* in the native *eGFP* (green, x-axis) and *GFP*-stained (red, y-axis) channels across animals (n = 3/4/4/4 *Dbh*^{cre}/*Net*^{cre}/*Th*^{cre}/ PRS×8 mice, respectively). 21.5 ± 15.3% more cells were detected in the GFP-stained channel as compared to the native eGFP channel (absolute difference: 20.5 ± 16.5 cells; t-test against 0: $t_{14} = 4.8$, $p = 2.8 \times 10^{-4}$). **c,** Distribution of normalized fluorescence in anti-GFP stained channel as a function of the normalized fluorescence in the native eGFP channel across cells. Fluorescence was averaged within each cell mask (detected in the GFP-stained channel), then binned into 50 × 50 equally spaced bins, and further smoothed by a 2D 10 × 10 boxcar function. The averaged normalized brightness of immune-stained cells per animal (0.40 ± 0.06) exceeded the averaged normalized brightness of the native eGFP-expressing cells (0.26 ± 0.06) by 55 ± 35% (absolute difference: 0.13 ± 0.076; t-test against 0: $t_{14} = 6.66$, $p = 1.08 \times 10^{-5}$). **d**, To quantify the difference in fluorescence between the anti-GFP immunostaining and native eGFP fluorescence in more details, we fitted a non-linear function describing the fluorescence of GFP-stained cells as a function of native eGFP fluorescence (after within-channel normalization, see panel c). The function is of the form $f'_R = \phi(\text{bias} + \text{gain} \times \phi^{-1}(f_G))$, where f_R and f_G denotes the fluorescence in the red (*GFP*-stained) and green (native *eGFP*) channels respectively, and ϕ corresponds to the normal cumulative distribution function. The 'bias' parameter quantifies the overall change in fluorescence induced by the immunostaining (top panel), while the 'gain' parameter accounts for a possible asymmetry in the fluorescence increase depending on the native *eGFP* fluorescence (bottom panel). **e**, Estimated parameter values from the function presented in **d**. The 'bias' parameter was significantly larger than 0, indicating an increase in fluorescence following *GFP*-staining (0.14 ± 0.19; t-test against 0: $t_{14} = 2.85$, $p = 0.013$). The 'gain' parameter was significantly smaller than 1, indicating that the increase in fluorescence was substantially stronger for the dimmest cells in the native *eGFP* channel (0.50 ± 0.17; t-test against 1: $t_{12} = -11.56$, $p = 1.5 \times 10^{-8}$). In **b**, **c**, and **f**, error bars denote the standard error of the mean (with n = 15), while statistical significance is denoted by */**/*** for $p < 0.05/0.01/0.001$, respectively.

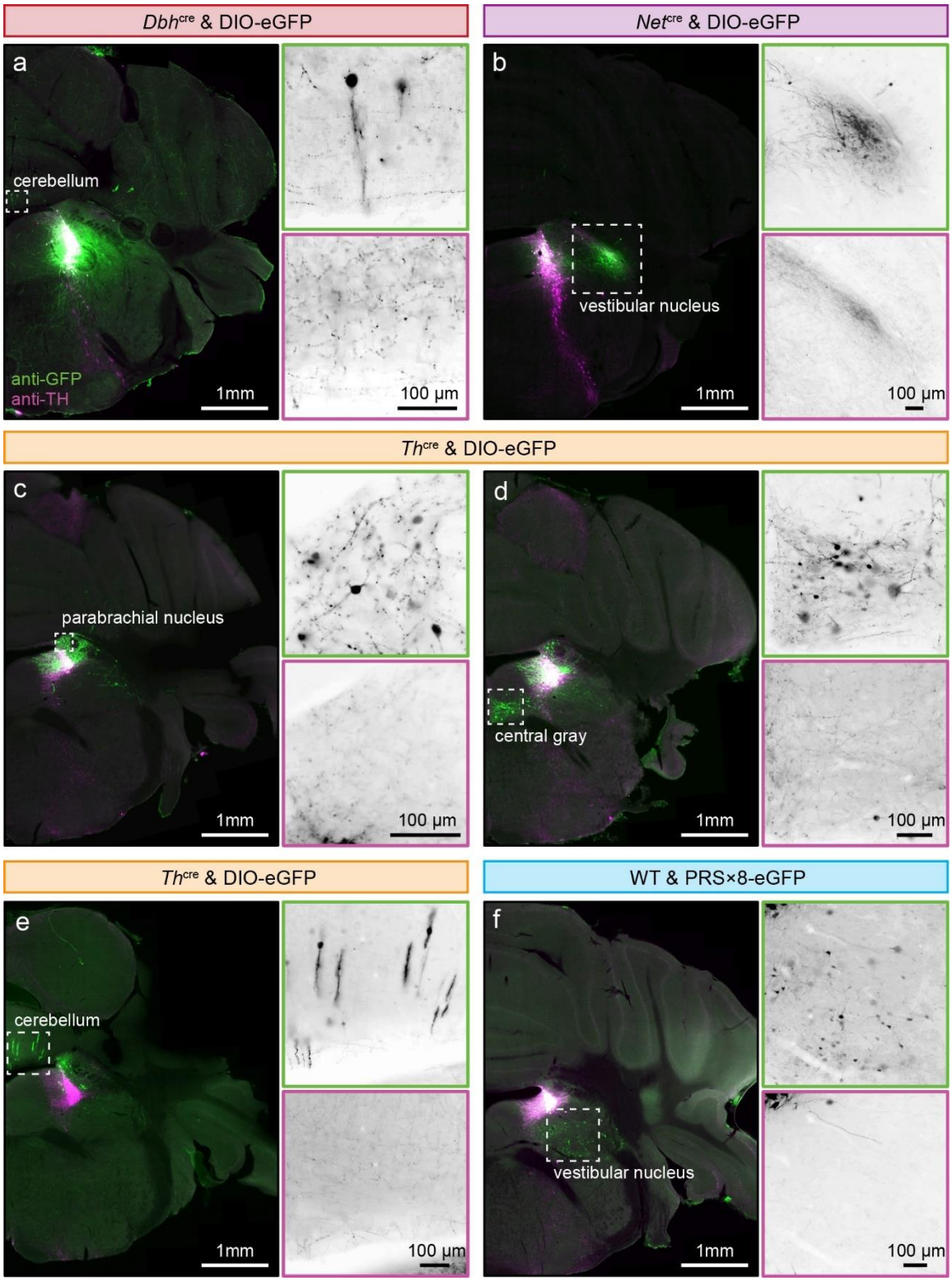

Figure S5 | Ectopic transgene expression across model systems. Example brain slices showing ectopic expression upon *Dbh*^{cre} (**a**), *Net*^{cre} (**b**), *Th*^{cre} (**c-e**), and PRS×8 (**f**) mediated transgene expression. Immuno-straining against TH and GFP is displayed in magenta and green respectively. Insets show inverted gray scale images for a better contrast.

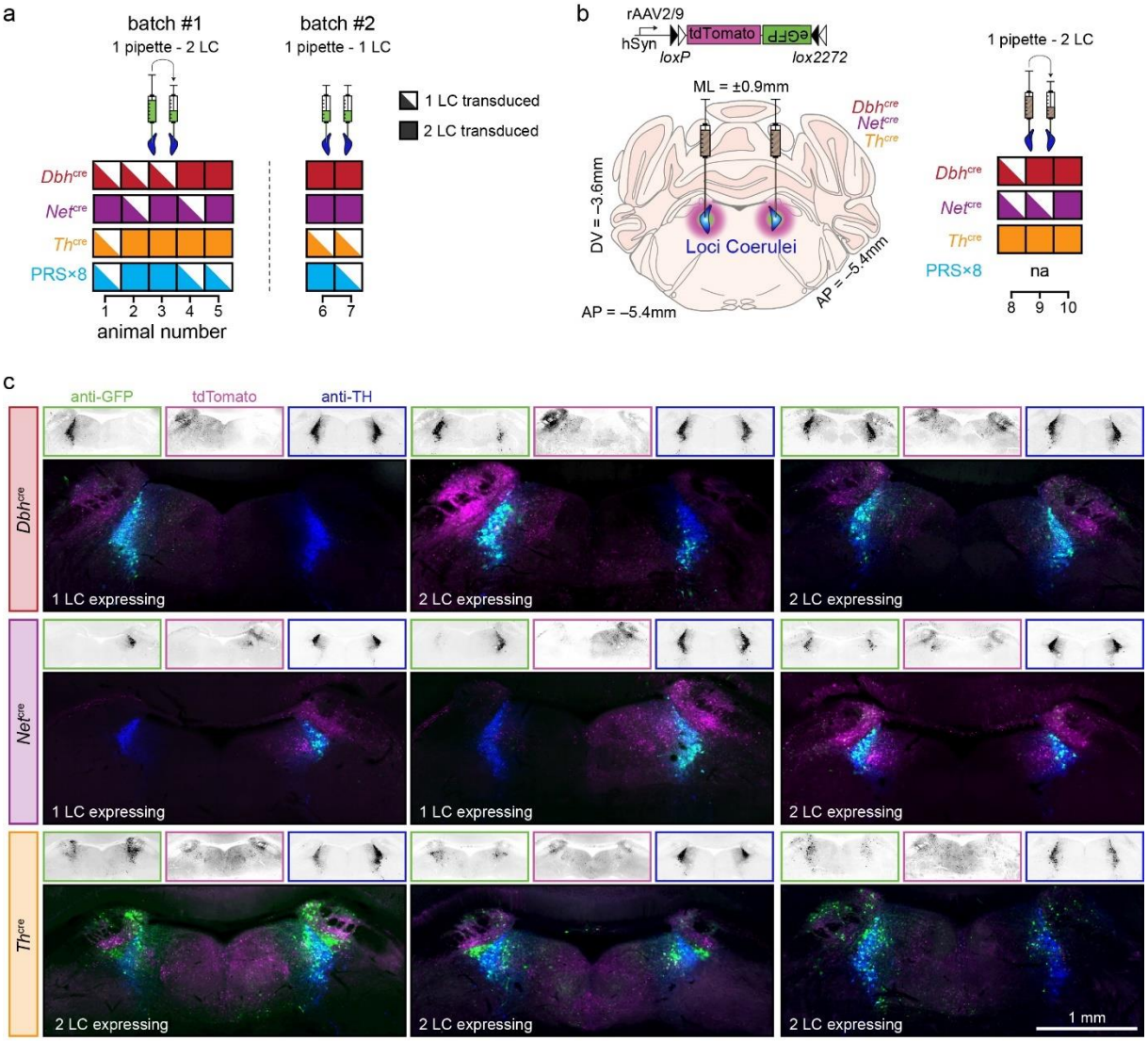

Figure S6 | Verification of LC transduction and estimation of viral spread. a, Fraction of animals with 1 or 2 LC transduced. In the first surgery batch (n = 5 animals in each group), a single micropipette was loaded with enough virus (2 × 300nL) to infect both LC; the micropipette was then used to inject the virus sequentially in each LC. In the second surgery batch (n = 2 animals in each group), one micropipette was used for each LC in order to control for possible differences in viral distribution, which might depend on the injection sequence and thereby explain failure in transducing one of the LC. With both approaches, cases of failed LC transduction were observed, suggesting they most likely followed from stereotactic targeting errors (with the pipette perhaps ending up in the 4th ventricle). **b**, Viral spread was verified by injections of a so-called 'cre-switch' construct leading to eGFP expression in a cre-dependent manner and tdTomato expression in cre-negative cells[36]. **c**, Transgene expression in *Dbh^{cre}*, *Net^{cre}* and *Th^{cre}* animals (n = 3 animals each) shows conditional eGFP expression in cre-expressing cells (green) and tdTomato expression in cre-negative cells (magenta). LC-NE cells are visualized by immunostaining against TH (dark blue). Importantly, in animals without eGFP expression, cre-negative cells around the LC also lacked the expression of tdTomato, suggesting absence of viral transduction in that hemisphere altogether (and likely loss of the virus suspension to the ventricle).

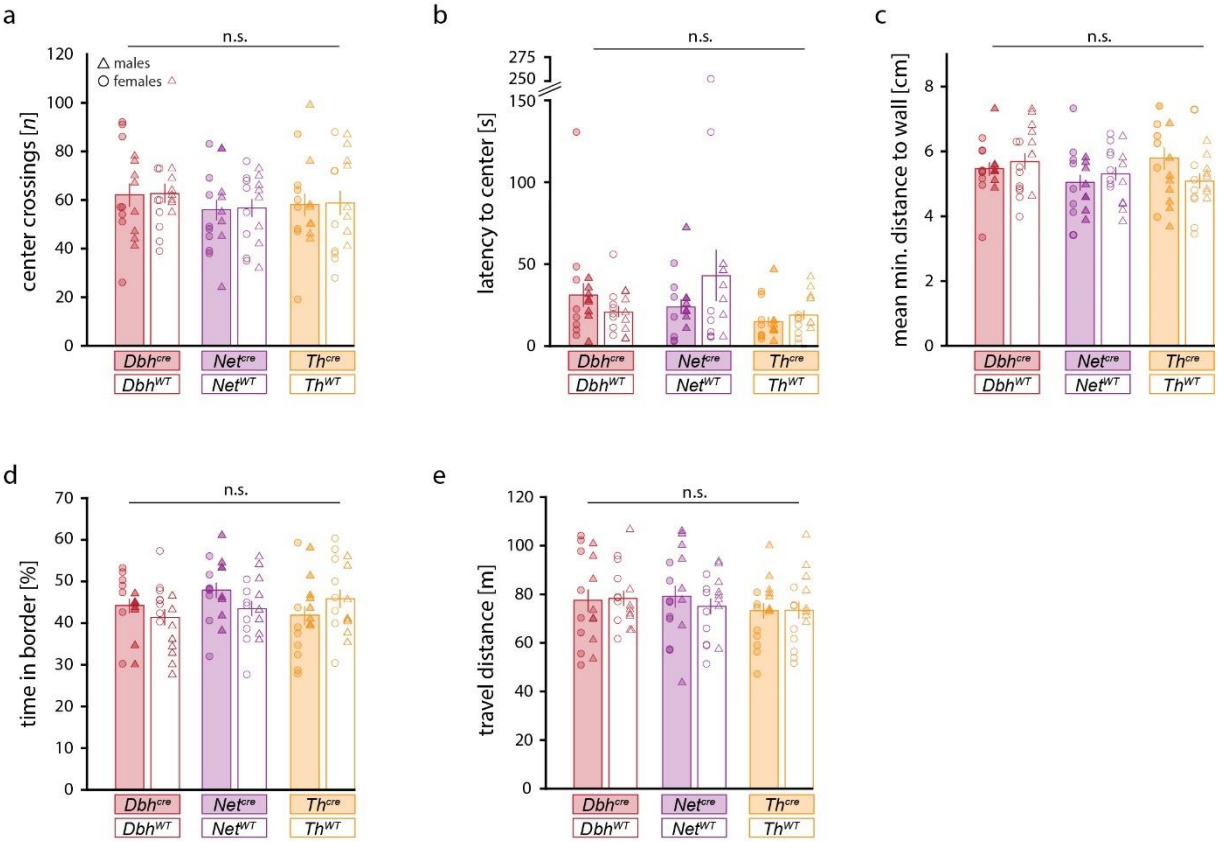

Figure S7 | Supplementary readouts obtained in the open field test. No effect of genotype could be detected on anxiety-like behavior as approximated by **(a)** the number of center crossings, **(b)** the latency to the first center crossing, **(c)** the mean minimum distance to the wall, **(d)** the percentage of time spent in the border of the arena, nor to general locomotion behavior as approximated by **(e)** the total distance travelled by the mouse. All data is depicted as mean ± standard error of the mean. n.s. = not significant. *n* = 8 females (circles) and 8 males (triangles).

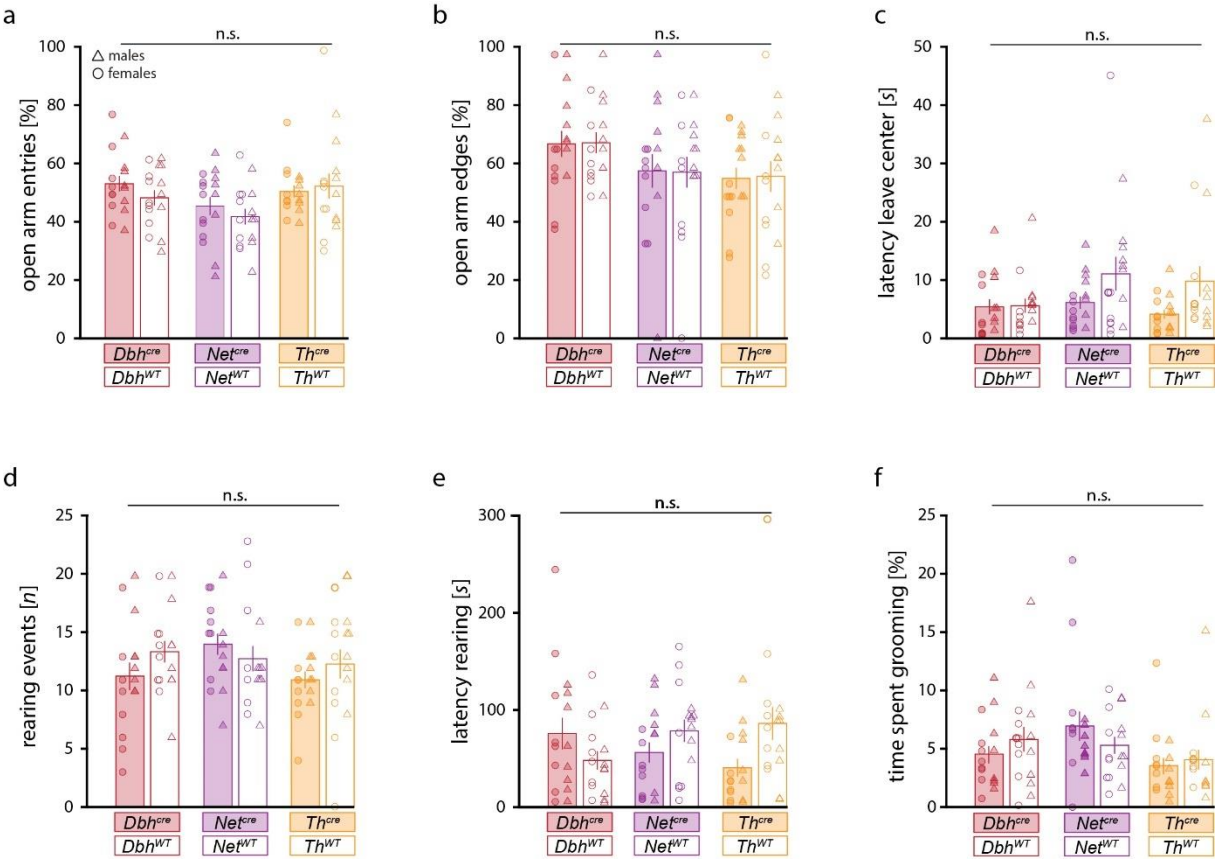

Figure S8 | Supplementary readouts obtained in the elevated plus maze. No effect of genotype could be detected on anxiety-like behavior as approximated by **(a)** the number of open arm entries, **(b)** the percentage of open arm entries on which the animal went to the distant edge of the arm, **(c)** the latency to leave the central platform, **(d)** the number of rearing events, **(e)** the latency to the first rearing event, or **(f)** the percentage of time spent grooming. All data is depicted as mean ± standard error of the mean. n.s. = not significant. *n* = 8 females (circles) and 8 males (triangles).

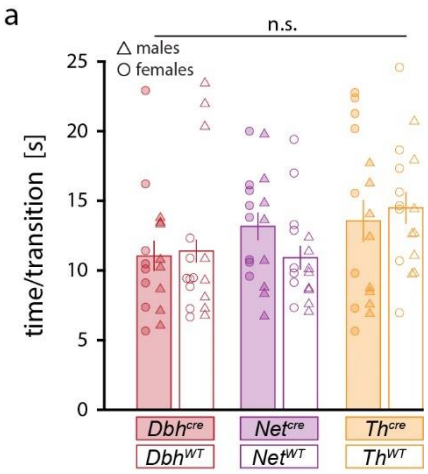

Figure S9 | Supplementary readouts obtained in the Y-maze. No effect of genotype could be detected on locomotion or explorative behavior as approximated by **(a)** the average time per transition between Y-maze arms. All data is depicted as mean ± standard error of the mean. n.s. = not significant. *n* = 8 females (circles) and 8 males (triangles).

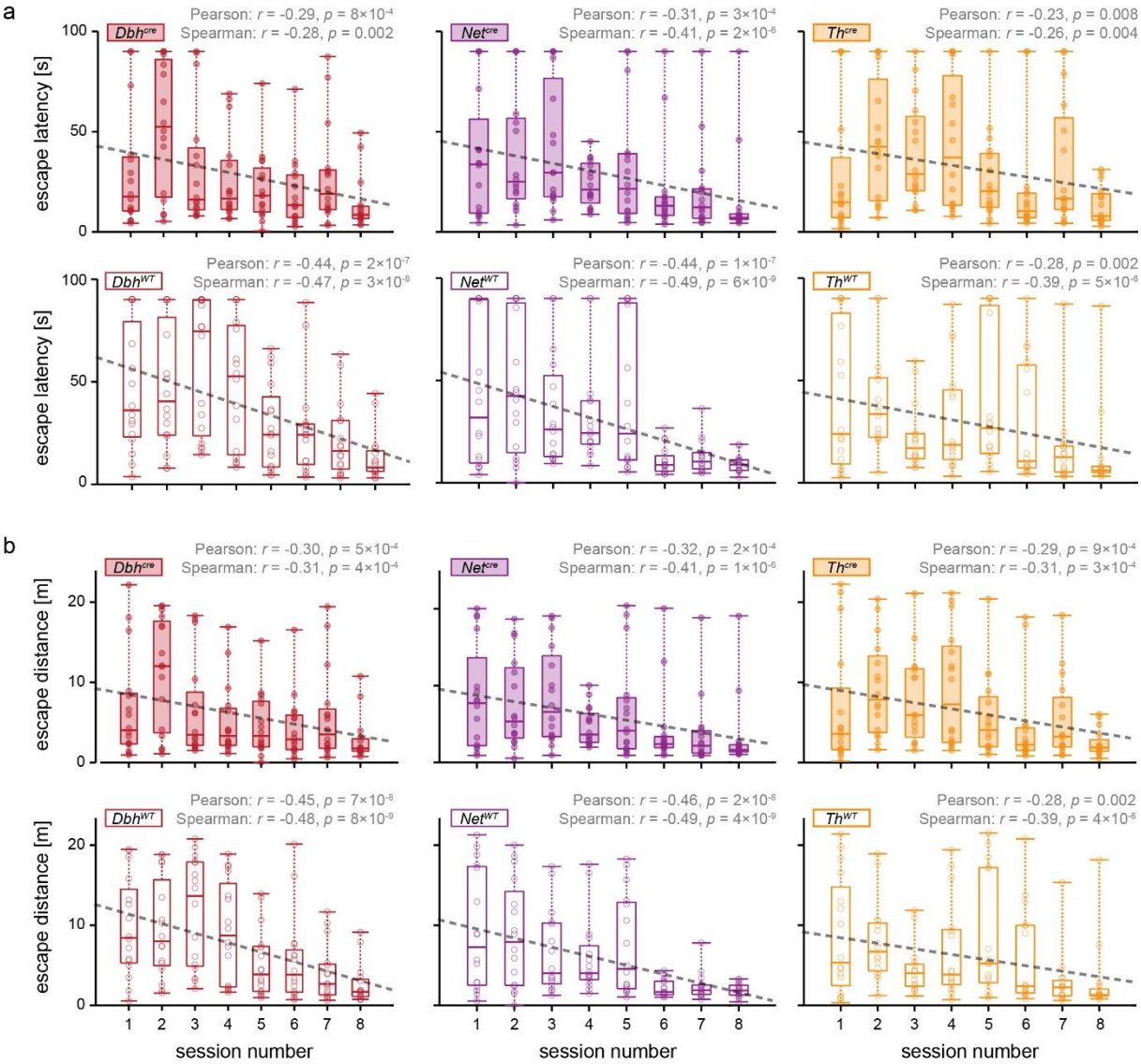

Figure S10 | Morris water maze during training sessions. In each group (n = 16 mice/group), both the latency to reach the platform **(a)** and the distance until the platform was reached **(b)** decreased as a function of training session number (4 sessions were performed on each day for two subsequent days), as indicated by both Pearson's and Spearman's correlation, indicating successful spatial learning in the water maze. Boxplots depict 0/25/50/75/100 percentiles, respectively. Dashed lines indicate the linear fit according to the method of least squares.

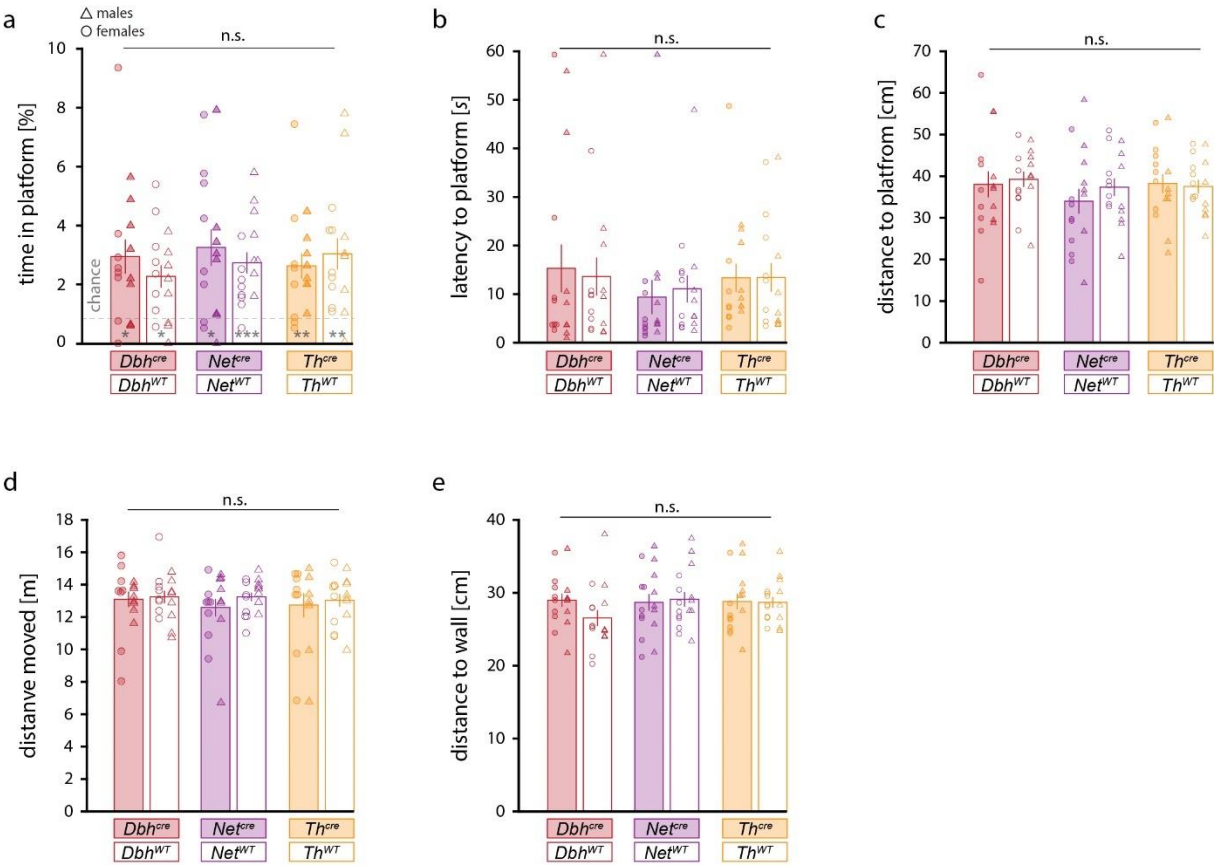

Figure S11 | Supplementary readouts obtained in the Morris water maze. No effect of genotype could be detected on spatial memory as approximated by **(a)** the time spent in the platform area, **(b)** the time needed to reach the platform, and **(c)** the mean minimal distance to the platform. No effect of genotype could be detected on locomotion behavior as approximated by **(d)** the total distance travelled. No effect of genotype could be detected on **(e)** the average distance to the wall, suggesting comparable thigmotactic behavior of mice. All data is depicted as mean ± standard error of the mean. n.s. = not significant. *n* = 8 females (circles) and 8 males (triangles). */**/***, depicted in panel a, for $p < 0.05/0.01/0.001$, respectively, tested against chance level.

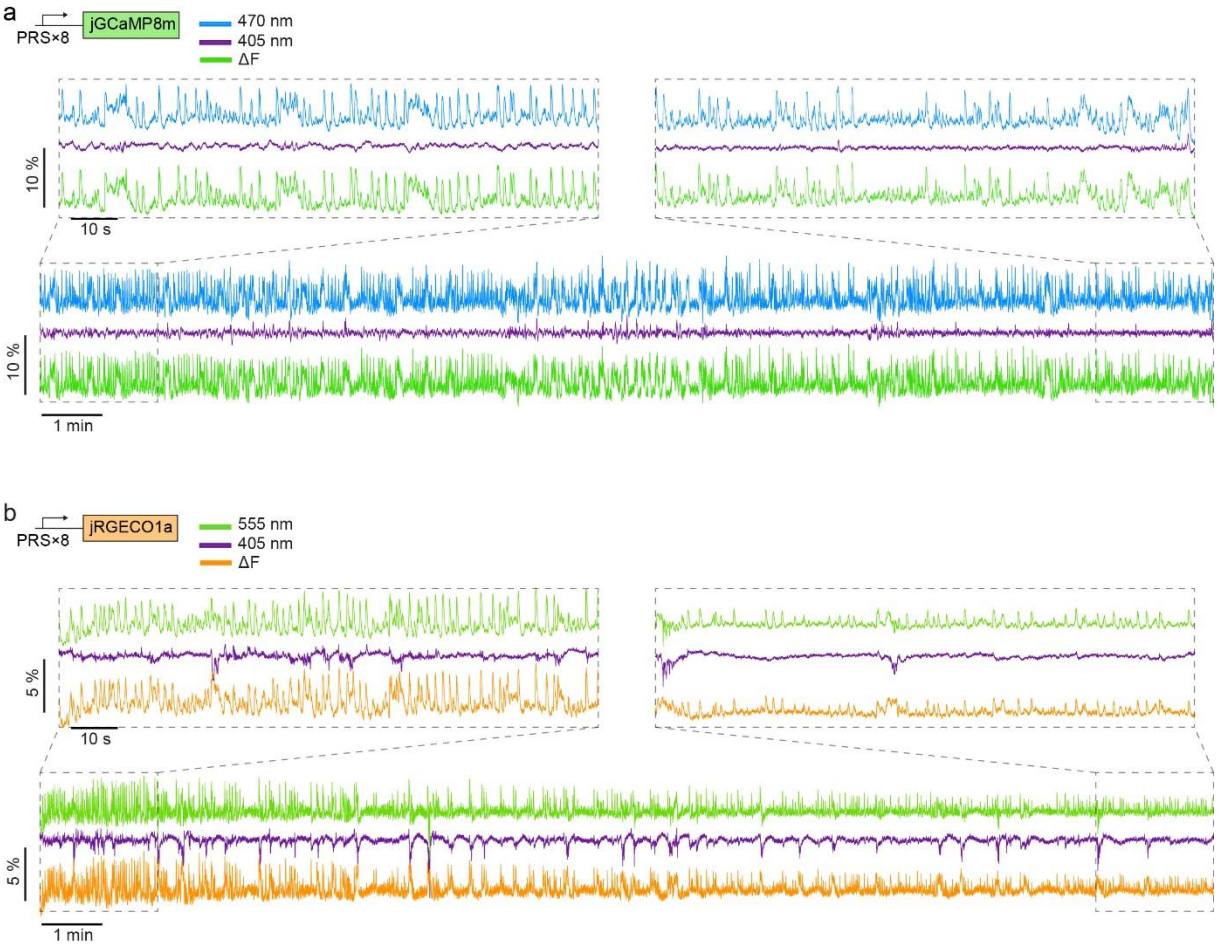

Figure S12 | Bleaching of calcium indicators in fiber photometry recordings from the LC. (a) Fluorescence traces of PRS×8-jGCaMP8m in LC-NE neurons with calcium-dependent excitation (blue) and quasi-isosbestic excitation (purple). The ΔF trace is shown in green. Traces are shown for a continuous recording period of 20 minutes (bottom). Insets show the first (top left) and last (top right) two minutes of the recording, respectively. **(b)** Fluorescence traces of PRS×8-jRGECO1a in LC-NE neurons with calcium-dependent excitation (green) and quasi-isosbestic excitation (purple). The ΔF trace is shown in orange. Traces are shown for a continuous recording period of 20 minutes (bottom). Insets show the first (top left) and last (top right) two minutes of the recording, respectively. Whereas the amplitude of transients is comparable in the first and last two minutes of the recording obtained from jGCaMP8m, substantial bleaching was observed in the case of jRGeco1a.